

Proposal for an autonomous quantum heat engine

Miika Rasola^{1*}, Vasilii Vadimov^{1†} Tuomas Uusnäkki¹ and Mikko Möttönen^{1,2‡}

1 QCD Labs, QTF Centre of Excellence, Department of Applied Physics, Aalto University, P.O. Box 13500, FI-00076 Aalto, Finland

2 QTF Centre of Excellence, VTT Technical Research Centre of Finland Ltd., P.O. Box 1000, 02044 VTT, Finland

* miika.rasola@aalto.fi, † vasilii.1.vadimov@aalto.fi, ‡ mikko.mottonen@aalto.fi

Abstract

We propose and theoretically analyse a superconducting electric circuit which can be used to experimentally realize an autonomous quantum heat engine. Using a quasiclassical, non-Markovian theoretical model, we demonstrate that coherent microwave power generation can emerge solely from the heat flow through the circuit determined by nonlinear circuit quantum electrodynamics. The predicted energy generation rate is sufficiently high for its experimental observation with contemporary techniques, rendering this work a significant step toward the first experimental realization of an autonomous quantum heat engine based on Otto cycles.

Copyright attribution to authors.

This work is a submission to SciPost Physics.

License information to appear upon publication.

Publication information to appear upon publication.

Received Date

Accepted Date

Published Date

Contents

1	Introduction	2
2	Device	3
2.1	The circuit	3
2.2	Initial assumptions and the recipe for solution	5
3	Theory	6
3.1	Equations of motion	6
3.1.1	Time-independent Green's function	9
3.2	Finding the Time-dependent Green's function	9
3.3	Averaging over noise and time	10
4	Numerical demonstration of an autonomous quantum heat engine	11
4.1	Energy generation rate	11
4.1.1	Power and efficiency	13
4.2	Parameter sweeps	14
4.3	Quantum disadvantage	17
4.4	Comparison to the Otto cycle	18
5	Conclusions	19

A	Deriving the optomechanical approximation	21
B	Simplification of the equations of motion	22
C	Numerical solution of the Green's function	23
D	Noise and time averages	24
E	Estimating efficiency	26
	References	28

1 Introduction

Superconducting quantum circuits provide one of the most versatile platforms for experimental implementation of various quantum technological concepts and devices [1]. The field of quantum microwave engineering, serving a purpose beyond fundamental research with the goal of realizing practically useful quantum devices [1, 2], has already produced numerous groundbreaking results in quantum computation [3–7], communication [8–11], simulation [12–18], and sensing [19–26].

As quantum technology evolves further, the necessity for understanding thermodynamics at the quantum level becomes of increasing and urgent importance. On the one hand, quantum thermodynamics [27–29] seeks to extend the theories of classical thermodynamics into the domain of single quantum systems in order to improve our understanding of microscopic and mesoscopic out-of-equilibrium systems with heat flows. On the other hand, the theoretical concept of a thermodynamic cycle, along with the heat engine that implements it, has been foundational to thermodynamics since its inception in the 19th century. Thus, it is not surprising that they remain indispensable in the quantum era.

Although microwave quantum engineering has led to significant breakthroughs in recent decades, only one experimental realization of a reciprocating quantum heat engine (QHE) in superconducting quantum circuits has been reported to date [30]. Another device capable of operating in the continuous QHE regime is reported in Ref. [31]. In contrast, numerous experimental demonstrations of QHEs have been achieved in microscopic atomic devices, such as single trapped ions [32], a spin coupled to single-ion motion [33, 34], nitrogen-vacancy centre interacting with a light field [35], nuclear magnetic resonance [36, 37], and large quasi-spin states of caesium impurities immersed in an ultracold rubidium bath [38]. However, there exists a substantial amount of experimental studies about heat conduction and thermodynamics in superconducting circuits exists, providing prospects for further advancement [39–44].

Autonomous quantum heat engines are of a class of particularly interesting thermal devices operating at the single quantum level and capable of autonomous operation, where they only utilize the flow of heat as a resource in order to provide useful work. All of the above-cited thermal machines are inherently non-autonomous because their thermodynamic cycles need to be persistently driven by some type of external control. In this case, it is very challenging to provide more work than the energy consumed for the external control and to even extract the work produced by the heat engine as it typically only exists superimposed on a macroscopic external control field.

Although superconducting quantum circuits have yet to flourish in the field of quantum

thermal machines, we consider that they offer a promising platform for realizing the first autonomous QHE which implements thermodynamic cycles. In this article, we build upon our previous work [45], where we proposed a general-level theoretical approach for realizing an autonomous QHE using an arbitrary system governed by an optomechanical Hamiltonian [46, 47] and coupled to two narrow-band thermal reservoirs [48]. Here, we focus on an experimentally feasible superconducting circuit and derive an in-depth theoretical model for it starting from the first principles, explicitly linking the circuit to the physical quantities defining its electrodynamics. Furthermore, we show that in a carefully constructed superconducting circuit, a resonator acting as the controller of the cycle can exhibit effectively negative internal dissipation, i.e., coherent microwave power generation, arising solely from the internal dynamics of the QHE and the corresponding heat flow through the circuit.

We stress that various theoretical proposals of QHEs, both in optomechanical systems and quantized superconducting circuits from other authors, precede this work. References [49–51] extensively analyse the possibility of realizing a coherently driven quantum Otto cycle in an optomechanical system, whereas Refs. [52–54] utilize optomechanical systems, but rely on periodic incoherent thermal drives. Hardal et al. [54] even propose a device based on superconducting circuits, but leave the discussion on a general level without specifying the circuit in detail. Furthermore, Refs. [55–57] study theoretical models of autonomous QHEs on the level of Markovian master equations. In contrast to these high-level theoretical proposals, we take the discussion closer to a readily designed device by analysing the circuit starting from the physical quantities defining the circuit. In addition, our proposed QHE is fully autonomous without any external persistent periodic thermal pumping or coherent drive. Finally, as opposed to the other approaches, our theoretical description is non-Markovian, taking into account the peaked shape of the reservoir spectra, which seems to be required to satisfactorily describe an autonomous QHE.

The article is organised as follows. In Sec 2, we define the circuit in detail, specifying the necessary physical quantities and parameters. We also outline the theoretical framework used to analyse the system, including the required approximations. In Sec. 3, we present a step-by-step derivation of the theoretical model, providing all relevant calculations before arriving at the final result. We then apply this model to a specific set of circuit parameters in Sec. 4, demonstrating that the circuit can operate as an autonomous quantum heat engine. By performing multiple parameter sweeps, we analyse the behaviour of the circuit and compare its dynamics to the quantum Otto cycle. Finally, in Sec. 5, we summarise our findings and discuss potential future research directions and applications for the proposed device.

2 Device

2.1 The circuit

Before delving into the theoretical details, let us first specify the circuit. In Fig. 1, we present a lumped-element circuit model for the QHE and assign the required physical quantities. The circuit consists of four inductor-capacitor (LC) resonators denoted as A, B, C, and H, each comprising of a capacitance, C_i , and an inductance, L_i , with $i = a, b, c, h$. In the following, we use the subscripts “h” and “c” for “hot” and “cold”, respectively. Resonators C and H, collectively referred to as the filters, contain dissipative elements at temperatures $T_c < T_h$, respectively, and act as the non-Markovian heat reservoirs with Lorentzian-shaped power spectral densities. The filters are linearly coupled to resonator A via the coupling capacitances C_{ha} and C_{ca} . The core of the QHE is formed by the coupled system of resonators A and B, where the non-linear coupling implemented by a SQUID enables the performance of the heat engine. The inductor

of resonator A is grounded through this symmetric SQUID, such that a part of the inductor of resonator B becomes a part of the SQUID loop, establishing the non-linear coupling between A and B.

In the context of a mechanical heat engine, resonator A can be viewed as the working fluid, and resonator B acts as a flywheel that facilitates work output. To provide intuition, one may also study an analogue to an internal combustion engine, where resonator A is considered as the piston of the combustion engine moving within the cylinder, and resonator B as the combination of the crank shaft and the flywheel.

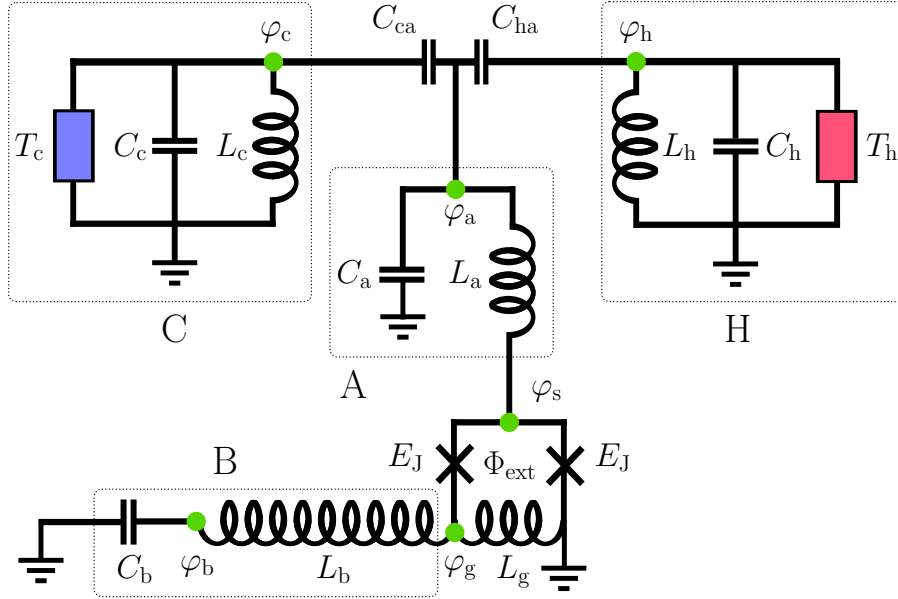


Figure 1: Lumped-element circuit model of the quantum heat engine. The heat engine circuit consists of four LC resonators denoted by A, B, C, and H as marked by the dotted line boxes. The main capacitances and inductances of the resonators are denoted by C_i and L_i , respectively, with $i = a, b, c, h$. The capacitances C_{ca} and C_{ha} couple resonator A to resonators C and H, respectively. Resonators C and H contain dissipative elements, indicated by the blue and red boxes, maintained at temperatures T_c and T_h , respectively. The Josephson junctions in the symmetric SQUID loop both have a Josephson energy of E_J , and Φ_{ext} denotes the static external magnetic flux threading the SQUID loop. In addition, a small piece of an inductor directly connected to resonator B with the inductance L_g forms a part of the SQUID loop, through which resonator B is also grounded. We indicate the circuit nodes with green dots, and assign a flux variable φ_i , with $i = a, b, c, h, s, g$, for each node.

In addition to the physical structure and quantities, we define six flux node variables [58, 59], one for each resonator and two auxiliary node variables, φ_s and φ_g , for the purpose of modelling the SQUID-mediated coupling correctly. First, we divide the field in resonator B into two components, but subsequently derive an effective-field approach unifying the two fields into a single equation of motion. The field φ_g can be identified as the coupling field, i.e., the part of resonator B that couples to the field φ_s . Similarly, φ_s represents a small deviation from φ_a , separated by the inductance L_a , that couples to φ_g via the SQUID. In the following, we will rigorously derive the equations of motion for these fields and show that the mode in resonator B can exhibit coherent microwave power generation arising solely from the internal dynamics of the device involving the heat flow from the hot to the cold reservoir.

2.2 Initial assumptions and the recipe for solution

As the final step in our preparation, we draw some initial assumptions about the parameters of the system necessary for achieving the desired QHE dynamics and outline the approach for modelling the system. The primary goal of this circuit is to achieve dynamics where resonator A undergoes a cycle analogous to the quantum Otto cycle [27, 60] driven by the field amplitude of resonator B. This concept, along with most of the assumptions made here, has been thoroughly discussed phenomenologically in Ref. [45]. Therefore, we will simply list the assumptions here without delving into detailed reasoning.

The first requirement, as mentioned above, is the existence of heat reservoirs at different temperatures: $T_c < T_h$. We have already assigned angular frequencies for the filter resonators, operating as pass-band filters between the corresponding dissipative elements and resonator A, but necessarily, the hot filter must have a higher frequency than the cold filter. In Ref. [45], the following condition for the angular frequency of resonator A is set: in the operational mode, the mean angular frequency of the working fluid, ω'_a , preferably lies between the filter frequencies, resulting in the condition $\omega_c \lesssim \omega'_a \lesssim \omega_h$. In the current circuit, ω'_a is an effective angular frequency of the subcircuit consisting of C_a , L_a , and the SQUID loop. By virtue of the SQUID, this frequency becomes flux-tunable and must be tuned to a suitable value by the external flux Φ_{ext} . Below, we find an approximate expression for ω'_a and show that, although the exact formulation of this condition differs slightly within the framework used here, its fundamental principle remains unchanged. For successful tuning, the frequency difference between the filter resonators desirably exceeds the capacitive coupling strength between the filters and resonator A arising from C_{ca} and C_{ha} . Lastly, we impose the condition that the angular frequency of resonator B is significantly lower than that of the other resonators: $\omega_b \ll \omega_c, \omega_a, \omega_h$ [45].

Our goal is to theoretically show that the dissipative dynamics of the circuit can lead to observable coherent microwave power generation in resonator B. To this end, we identify three characteristic time scales in the system: the short time scale governed by the high frequencies ω_a , ω_h , and ω_c , the intermediate scale associated with the frequency ω_b , and the long time scale, determined by the rate at which the average occupation or field amplitude in resonator B changes. The rate of energy generation is proportional to the long time scale. We shall further assume that the rate of generation is considerably lower than the angular frequency of resonator B, ω_b , which effectively allows using the Wentzel–Kramers–Brillouin (WKB) approximation [61] for the resonator mode ϕ_b . Based on this assumption, we systematically eliminate all other degrees of freedom except those of the mode in resonator B, ultimately arriving at an equation of motion for the amplitude and phase of the mode in resonator B.

In order to facilitate simultaneous modelling of both non-linear and non-Markovian properties of the circuit, we resort to a quasiclassical theoretical model. We model the noise spectral density by the quantum mechanical result, but treat the circuit degrees of freedom classically. Since a linear system retains the form of its equations of motion in quantization, and we assume the non-linear component to be a small perturbation to the linear dynamics, we expect that the quasiclassical model satisfactorily describes the system.

3 Theory

3.1 Equations of motion

Excluding the SQUID and the dissipative components, the classical Lagrangian for the circuit described in Fig. 1 is given by

$$\mathcal{L}_R = \frac{C_{\Sigma a} \dot{\varphi}_a^2}{2} - \frac{(\varphi_a - \varphi_s)^2}{2L_a} + \frac{C_b \dot{\varphi}_b^2}{2} - \frac{(\varphi_b - \varphi_g)^2}{2L_b} + \sum_{f=c,h} \left[\frac{C_{\Sigma f} \dot{\varphi}_f^2}{2} - \frac{\varphi_f^2}{2L_f} + C_{fa} \dot{\varphi}_a \dot{\varphi}_f \right], \quad (1)$$

where we define the capacitance sums $C_{\Sigma a} = C_a + C_{ha} + C_{ca}$ and $C_{\Sigma f} = C_f + C_{fa}$. Neglecting the capacitance of the Josephson junctions, the Lagrangian, including the elements in the SQUID loop providing the coupling between resonators A and B, is given by

$$\mathcal{L}_S = -\frac{\varphi_g^2}{2L_g} + E_J \cos\left(\frac{2\pi\varphi_s}{\Phi_0}\right) + E_J \cos\left[\frac{2\pi}{\Phi_0}(\varphi_s - \varphi_g - \Phi_{\text{ext}})\right], \quad (2)$$

where $E_J = I_c \Phi_0 / (2\pi)$ is the Josephson energy of the junctions with the critical current I_c and the magnetic flux quantum $\Phi_0 = \pi \hbar / e$, defined by the reduced Planck constant, \hbar , and the elementary charge, e . The total Lagrangian of the circuit without any additional approximations is thus given by the sum $\mathcal{L} = \mathcal{L}_R + \mathcal{L}_S$.

Typically, the trigonometric potential in the SQUID Lagrangian is Taylor expanded up to the first non-linear correction. Before such treatment, we need to ensure that the field variables in the cosine are sufficiently small. To this end, we find the minimum of the potential energy related to the above SQUID loop Lagrangian (2), and define new shifted field variables as deviations from the potential minimum for the fields inductively coupled to the SQUID. The new field variables are given as $\tilde{\varphi}_i = \varphi_i - \varphi_g^{(0)}/2$, where $i \in [s, a, b, g]$, and $\varphi_g^{(0)}$ is the field at the potential minimum, given by the equation

$$\frac{\varphi_g^{(0)} - \Phi_{\text{ext}}}{L_g} + 2I_c \sin\left(\frac{\pi}{\Phi_0} \varphi_g^{(0)}\right) = 0. \quad (3)$$

The above equation is transcendental and, in general, needs to be solved numerically. We observe that this equation has a single solution if $I_c L_g < \Phi_0 / (2\pi)$, which is well satisfied in our circuit.

Consequently, the approximated SQUID loop Lagrangian in terms of the shifted fields reads

$$\mathcal{L}'_S = -\left(\frac{1}{2L_J} + \frac{1}{2L_g}\right) \tilde{\varphi}_g^2 - \frac{\tilde{\varphi}_s^2}{L_J} + g_0^2 \tilde{\varphi}_g \tilde{\varphi}_s^2, \quad (4)$$

where we define the optomechanical coupling constant and the Josephson inductance, respectively, as

$$g_0^2 = \frac{4I_c \pi^2}{\Phi_0^2} \sin\left(\frac{\pi}{\Phi_0} \varphi_g^{(0)}\right), \quad (5)$$

$$L_J^{-1} = \frac{4I_c \pi}{\Phi_0} \cos\left(\frac{\pi}{\Phi_0} \varphi_g^{(0)}\right). \quad (6)$$

The details of this calculation and the following series expansion, along with the appropriate approximations, are carried out in Appendix A. This approximate Lagrangian \mathcal{L}'_S replaces \mathcal{L}_S in the full Lagrangian which hence becomes $\mathcal{L}' = \mathcal{L}_R + \mathcal{L}'_S$. Note that the resonator Lagrangian (1) retains its original form even though the field variables are replaced by the shifted fields.

The equations of motion corresponding to \mathcal{L}' are obtained by direct application of the Euler–Lagrange equation, which results in

$$\ddot{\tilde{\varphi}}_a + \omega_a^2 (\tilde{\varphi}_a - \tilde{\varphi}_s) + \sum_{f \in [h, c]} \alpha_{fa} \ddot{\varphi}_f = 0, \quad (7a)$$

$$\frac{\tilde{\varphi}_a - \tilde{\varphi}_s}{L_a} - \frac{2\tilde{\varphi}_s}{L_J} + 2g_0^2 \tilde{\varphi}_s \tilde{\varphi}_g = 0, \quad (7b)$$

$$\ddot{\tilde{\varphi}}_b + \frac{\tilde{\varphi}_b - \tilde{\varphi}_g}{C_b L_b} = 0, \quad (7c)$$

$$\left(\frac{1}{L_b} + \frac{1}{L_g} + \frac{1}{L_J} \right) \tilde{\varphi}_g - \frac{\tilde{\varphi}_b}{L_b} - g_0^2 \tilde{\varphi}_s^2 = 0, \quad (7d)$$

$$\ddot{\varphi}_f + \omega_f^2 \varphi_f + 2\gamma_f \dot{\varphi}_f + \alpha_f \ddot{\varphi}_a = \xi_f(t), \quad (7e)$$

where $f = h, c$ for hot and cold filter resonator, respectively, we define the angular frequencies $\omega_a = 1/\sqrt{C_{\Sigma a} L_a}$ and $\omega_f = 1/\sqrt{C_{\Sigma f} L_f}$, and the dimensionless coupling constants $\alpha_{fa} = C_{fa}/C_{\Sigma a}$ and $\alpha_f = C_{fa}/C_{\Sigma f}$, the filter dissipation rate $\gamma_f = 1/(2R_f C_{\Sigma f})$, along with the noise source function $\xi_f(t)$ due to the thermal environment [62], characterized by the power spectral density [63]:

$$S_f(\omega) = \int_{-\infty}^{\infty} \langle \xi_f(t + \tau) \xi_f^*(t) \rangle e^{i\omega\tau} d\tau = 4\hbar\omega\gamma_f^2 R_f \coth\left(\frac{\hbar\omega}{2k_B T_f}\right), \quad (8)$$

where T_f is the temperature of the heat reservoir, and k_B is the Boltzmann constant. Above, we formally define γ_f in terms of the resistance R_f , serving as the source of thermal noise in the filter resonator. Since the resistance can be chosen freely, γ_f effectively becomes a free parameter. Moving forward, we will treat γ_f as a fundamental parameter and infer the corresponding resistance when necessary.

As stated above, our primary focus lies in the evolution of the field $\tilde{\varphi}_b$. To this end, we aim to reduce the above set of equations by integrating out the other degrees of freedom. First, we solve $\tilde{\varphi}_g$ from Eq. (7d) in the time domain and insert the solution into Eqs. (7b) and (7c). In accordance with the approximations in Appendix A, we drop the resulting third-order terms. Next, we solve $\tilde{\varphi}_f$ from Eq. (7e) via Fourier transformation and insert the solution into the Fourier transformed Eq. (7a). The resulting equation for $\tilde{\varphi}_a$ in Fourier space is then solved, and the solution is substituted back into Eq. (7b), thus reducing the number of equations to two. To proceed, we redefine the units in the two remaining equations to render the field variables dimensionless. We obtain the relation $\tilde{\varphi}_{s/b} = (\Phi_0/\pi)\phi_{s/b}$. The details of the above derivation can be found in Appendix B. After these steps, we express the equations of motion governing the time evolution of the fields ϕ_b and ϕ_s as

$$\omega_s^2 \phi_s(t) + 2g_s^2 \phi_s(t) \phi_b(t) - \int_{-\infty}^{\infty} \mathcal{K}(t - \tau) \phi_s(\tau) d\tau = \xi(t), \quad (9)$$

$$\ddot{\phi}_b(t) + \omega_b^2 \phi_b(t) - g_b^2 \phi_s^2(t) = 0, \quad (10)$$

where the angular frequencies are defined as $\omega_s^2 = (1 + 2L_a/L_J) \omega_a^2$ and $\omega_b^2 = (1 - N_L)/(L_b C_b)$, with $N_L = (1 + L_b/L_g + L_b/L_J)^{-1}$, and the non-linear coupling constants are given by

$$g_s^2 = \frac{\Phi_0 g_0^2}{\pi C_{\Sigma a} N_L}, \quad g_b^2 = \frac{\Phi_0 g_0^2}{\pi C_b N_L}, \quad (11)$$

and the total noise source function $\xi(\omega)$ and the memory kernel $\mathcal{K}(\omega)$ are defined, in the frequency domain, as

$$\xi(\omega) = \frac{\omega_a^2 \sum_f \wp_f(\omega) \xi_f(\omega)}{\omega_a^2 - \omega^2 \left[1 + \sum_f \alpha_f \wp_f(\omega) \right]}, \quad (12)$$

$$\mathcal{K}(\omega) = \frac{\omega_a^4}{\omega_a^2 - \omega^2 \left[1 + \sum_f \alpha_f \wp_f(\omega) \right]}, \quad (13)$$

where

$$\wp_f(\omega) = \frac{\alpha_f \omega^2}{\omega_f^2 - \omega^2 - 2i\gamma_f \omega}. \quad (14)$$

See Appendix B for the details of obtaining these definitions.

Above, we have reduced the original set of equations of motion into two equations by integrating out the noise-driven filter modes along with φ_a , and consolidating the two modes within resonators B. We are left with Eq. (9), describing the dynamics at the node coupling the SQUID to resonator A, and Eq. (10), governing the dynamics of resonator B. Note that Eq. (10) retains the form of a harmonic oscillator equation, while Eq. (9) is governed by the memory kernel $\mathcal{K}(\omega)$ and the noise source $\xi(\omega)$. Let us define the effective frequency of the flux-tunable resonator consisting of resonator A and the SQUID termination, ignoring resonator B, as depicted in Fig. 1. Using the above-given external-flux dependent Josephson inductance, we can define $\omega'_a = 1/\sqrt{C_{\Sigma a}(L_a + L_J/2)}$, which is the frequency to be tuned to the operational range, given by $\omega_c < \omega'_a < \omega_h$, as mentioned in Sec. 2.

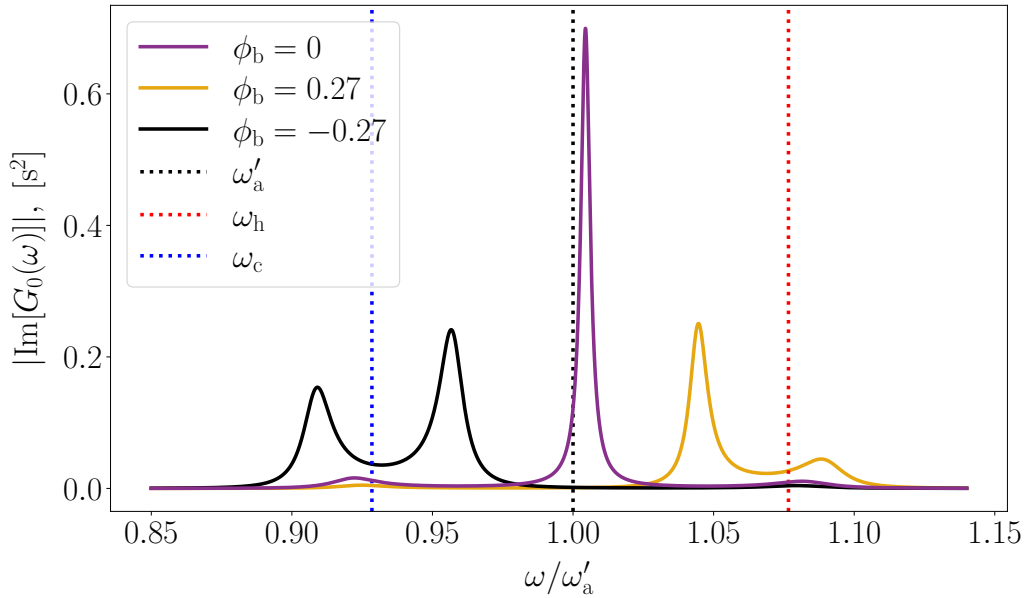


Figure 2: Absolute value of the imaginary part of the time-independent Green's function $G_0(\omega)$ of the SQUID mode as a function of angular frequency at different time-independent values of ϕ_b . The red and blue vertical dashed lines represent the bare frequencies of hot and cold filters, respectively, while the black dashed line shows the flux tunable angular frequency ω'_a , defined in the main text. We demonstrate the dependence of the Green's function on ϕ_b by using the values $\phi_b \in \{0, \pm 0.27\}$. The parameters used for these results are listed in Table 1.

3.1.1 Time-independent Green's function

Our next step is to integrate out the remaining high-frequency components in the system by solving Eq. (9) for ϕ_s . Before attempting a solution to Eq. (9), let us try to gain some intuition into the equation and the implied dynamics by examining its structure. By assuming the field ϕ_b is a time-independent constant, we recover the time-independent Green's function for Eq. (9) in the frequency domain as

$$G_0(\omega) = [\omega_s^2 + 2g_s^2\phi_b - \mathcal{K}(\omega)]^{-1}. \quad (15)$$

In Fig. 2, we show the absolute value of the imaginary part of the above Green's function at different values of ϕ_b . We observe the peaks related to each of the modes ϕ_s , ϕ_b , and ϕ_c , slightly offset from their estimated bare values due to their coupling energies. As expected, the peak associated with ϕ_s is clearly the strongest. The mode ϕ_s serves as an auxiliary mode, housed by resonator A, to model the SQUID-mediated coupling between resonators A and B. The coupling to the filters is mediated by the mode ϕ_a , and further weakened by the relatively weak capacitive coupling. We demonstrate the effect of the field ϕ_b on Eq. (9) by showing the Green's function with $\phi_b = 0$ and ± 0.27 . As alluded to in Sec. 2, the phenomenological notion of ϕ_b modulating the frequency of resonator A between the filter frequencies is clearly evinced here. Depending on the value of ϕ_b , the peak related to ϕ_s moves towards the corresponding filter peak. We also observe a slight repulsion from the filter peak, causing it to shift further away from the ϕ_s peak as it approaches.

3.2 Finding the Time-dependent Green's function

Equation (9) is a time-non-local integral equation with a peaked-spectrum noise function as the source term. We therefore employ Green's function methods to find the solution for an arbitrary source. We treat the left side of the equation (9) as a differential operator, so that the Green's function obeys the following equation:

$$[\omega_s^2 + 2g_s^2\phi_b(t)]G(t, t') - \int_{-\infty}^{\infty} \mathcal{K}(t - \tau)G(\tau, t') d\tau = \delta(t - t'). \quad (16)$$

The above equation is challenging to solve due to the time dependence of $\phi_b(t)$, and its closed-form solution remains unavailable in the general case. In order to proceed, we express the field variable ϕ_b as

$$\phi_b(t) = 2A_b(t) \cos[\omega_b t + \theta_b(t)], \quad (17)$$

where $A_b(t)$ and $\theta_b(t)$ are the time-dependent amplitude and phase of the field, respectively. In the following computation, we invoke the approximation of slow temporal evolution of $A_b(t)$ and $\theta_b(t)$. This is formally expressed as the assumption that the evolution rates are much lower than the inverse of the heat bath correlation time: $\dot{A}_b, \dot{\theta}_b \ll \gamma_f$. In practice, however, this simply means that we ignore the time dependence of $A_b(t)$ and $\theta_b(t)$ in solving the Green's function. To proceed, we transform the equation into the Fourier space by writing the Green's function in a doubly Fourier-transformed form,

$$G(t, t') = \frac{1}{2\pi} \iint_{-\infty}^{\infty} G(\omega, \omega') e^{-i\omega t + i\omega' t'} d\omega d\omega', \quad (18)$$

and substitute it in Eq. (16) taking care of the time-dependent term of ϕ_b . We arrive at the following equation

$$[\omega_s^2 - \mathcal{K}(\omega)]G(\omega, \omega') + 2g_s^2 A_b [e^{-i\theta_b} G(\omega - \omega_b, \omega') + e^{i\theta_b} G(\omega + \omega_b, \omega')] = \delta(\omega - \omega'). \quad (19)$$

To facilitate numerical solutions, let us reformulate the problem as a matrix equation. Specifically, we look for solutions in the vicinity of the integer multiples of the angular frequency, ω_b , in Fourier space. To this end, we express the Green's function in a form

$$G(\omega, \omega') = \sum_n G_n(\omega) \delta(\omega - \omega' - n\omega_b). \quad (20)$$

By substituting this ansatz into Eq. (19), one arrives at

$$\sum_n [P(\omega + n\omega_b)G_n(\omega) + R^*(\theta_b)G_{n-1}(\omega) + R(\theta_b)G_{n+1}(\omega)] = \delta_{n,0}, \quad (21)$$

where $P(\omega) = \omega_s^2 - \mathcal{K}(\omega)$ and $R(\theta_b) = 2g_s^2 A_b e^{i\theta_b}$. This formulation produces a system of equations, with each index n corresponding to one equation. The entire system can be expressed as a matrix equation, which can be solved efficiently numerically (see Appendix C). By solving the matrix equation to a sufficient degree in n , a large enough set of coefficients $G_n(\omega)$ in the series representation of the Green's function can be determined, allowing accurate evaluation of the Green's function. In this work, we set the range $n \in [-1000, 1000]$ for all computations, which is more than enough for reaching convergence. Once the Green's function is known, one can solve the equation (9) for an arbitrary source $\xi(\tau)$:

$$\phi_s(t) = \int_{-\infty}^{\infty} G(t', t) \xi(t') dt'. \quad (22)$$

3.3 Averaging over noise and time

Considering equation (10), we note that we are not actually interested in ϕ_s , but rather its square. Furthermore, as mentioned above, the characteristic frequency of the oscillations of $\phi_{s/a}$ is far off-resonant, and at a much higher frequency, as compared to the oscillations of ϕ_b . In addition, despite ϕ_s is a pure noise with zero average, its square has a non-vanishing expectation value. Neglecting the high-frequency fluctuations around this mean value, we replace the ϕ_s^2 appearing in Eq. (10) by its expectation value over noise realizations, thus creating a noise-averaged equation for the field ϕ_b , given as

$$\ddot{\phi}_b + \omega_b^2 \phi_b + 2\gamma_b \dot{\phi}_b - g_b^2 \langle \phi_s^2 \rangle_{\xi}(t) = 0, \quad (23)$$

where we have introduced dissipation into the equation, determined by the dissipation rate γ_b . This allows studying the effects of varying loss rates, including the effect of power output when the work done by the QHE is utilized.

Next, we use the expression (17) once more by inserting it into the above equation, and time averaging over one period of the mode ϕ_b . Here, we consider a single Fourier harmonic of $\langle \phi_s^2 \rangle_{\xi}(t)$ resonant to the mode ϕ_b . At this point, we invoke the final assumption regarding the time scales of the system: the field amplitude $A_b(t)$ evolves slowly in time compared with the oscillation frequency ω_b . To simplify the equation and to focus on the leading-order behaviour, we neglect all second-order derivatives, products of derivatives, and other small terms in the spirit of the WKB approximation [61]. Subsequently, we decompose the result into its real and imaginary components, yielding separate coupled equations of motion for the amplitude and phase, given as

$$\dot{A}_b(t) + \gamma_b A_b(t) + \frac{g_b^2}{2\omega_b} \text{Im}[\langle \phi_s^2 \rangle_{\xi,t}(A_b, \theta_b)] = 0, \quad (24)$$

$$A_b(t) \dot{\theta}_b(t) + \frac{g_b^2}{2\omega_b} \text{Re}[\langle \phi_s^2 \rangle_{\xi,t}(A_b, \theta_b)] = 0, \quad (25)$$

where

$$\langle \phi_s^2 \rangle_{\xi,t}(A_b, \theta_b) = \frac{1}{2\pi} e^{i\theta_b} \int_{-\infty}^{\infty} \sum_n G_n(\omega) G_{n-1}^*(\omega) S(\omega) d\omega, \quad (26)$$

is given in terms of the Green's function coefficients $G_n(\omega)$, the dependence of which on A_b and θ_b is visible in Eq. (21). The details of this calculation, along with the associated approximations, are provided in Appendix D. This expression can be evaluated efficiently numerically by the method described above. The equations of motion, Eqs. (24) and (25), yield the dynamics of resonator B at the slowest time scale of the circuit. We proceed with the analysis of their solution in the next section.

4 Numerical demonstration of an autonomous quantum heat engine

4.1 Energy generation rate

As explained in the beginning, our primary focus is to determine whether the proposed circuit can induce coherent generation of microwaves in resonator B and to identify the conditions under which this occurs. Although Eq. (24) needs to be solved numerically in general, its simple structure allows us to obtain certain results without explicitly solving it. Considering Eq. (24) as a generalized Langevin equation [64], we can define the amplitude-dependent total dissipation rate as

$$\Gamma_{\text{tot}}(A_b, \theta_b) = \gamma_b + \frac{g_b^2}{2A_b\omega_b} \text{Im} \left[\langle \phi_s^2 \rangle_{\xi,t}(A_b, \theta_b) \right]. \quad (27)$$

From this, we observe that when the total dissipation rate is positive, the amplitude decays in time. In contrast, a negative total dissipation rate causes the amplitude to grow. This is the condition for coherent microwave generation. Here, we refer to γ_b as the intrinsic dissipation rate since it contains all the sources of dissipation, be it internal or external, apart from the effect of the average noise pressure induced by the coupling to resonator A. In addition, we define the intrinsic quality factor as $Q_b = \omega_b/\gamma_b$.

Table 1: Physical parameters of the circuit used in the simulations herein. In the left section, we provide the values of the elementary parameters of the circuit labelled in Fig. 1, and the right section gives the derivative parameters defined throughout the main text.

Elementary parameters				Derivative parameters			
L_a	0.55 nH	C_a	0.18 pF	$\omega_a/(2\pi)$	15 GHz	$\omega'_a/(2\pi)$	10.03 GHz
L_h	0.75 nH	C_h	0.27 pF	$\omega_h/(2\pi)$	11.0 GHz	$\omega_s/(2\pi)$	20.2 GHz
L_c	1.03 nH	C_c	0.37 pF	$\omega_c/(2\pi)$	8.03 GHz	L_J	1.36 nH
L_b	0.78 nH	C_b	0.2 nF	$\omega_b/(2\pi)$	379 MHz	N_L	0.103
L_g	96.5 pH	C_{ha}	9.5 fF	α_h	0.034	α_{ha}	0.046
I_c	0.8 μ A	C_{ca}	16.1 fF	α_c	0.042	α_{ca}	0.078
T_c	10 mK	$\gamma_{h/c}$	$\omega_{h/c}/85$	g_0	$44.5 \sqrt{A}/Wb$	g_b	$0.66 \times \omega_b$
T_h	300 mK	Φ_{ext}	$0.5253 \times \Phi_0$	$\varphi_g^{(0)}$	$0.45 \times \Phi_0$	g_s	$0.52 \times \omega_a$

First and foremost, we verify that there exists a range of parameters that enables a negative total dissipation rate. In Fig. 3(a), we show the total dissipation rate, given by Eq. (27) as a

function of A_b for various intrinsic quality factors Q_b and other parameter given in Table 1. Notably, the total dissipation rate can become locally negative within a certain range of A_b , depending on the intrinsic dissipation rate. Moreover, the total dissipation rate reaches large enough negative values to facilitate its feasible experimental observation. For example, the curve corresponding to an intrinsic quality factor of $Q_b = 13600$, which is not a very high internal quality factor by modern standards [65–69], still reaches negative values. Note that the parameters of Table 1 used here are not optimized for maximum negative dissipation rates, but roughly chosen to provide maximum power output, as explained below. It is possible to obtain even higher negative total dissipation rates at the cost of lowering the output power. Nevertheless, the parameters of Table 1 are applied to all subsequent computations unless otherwise explicitly stated.

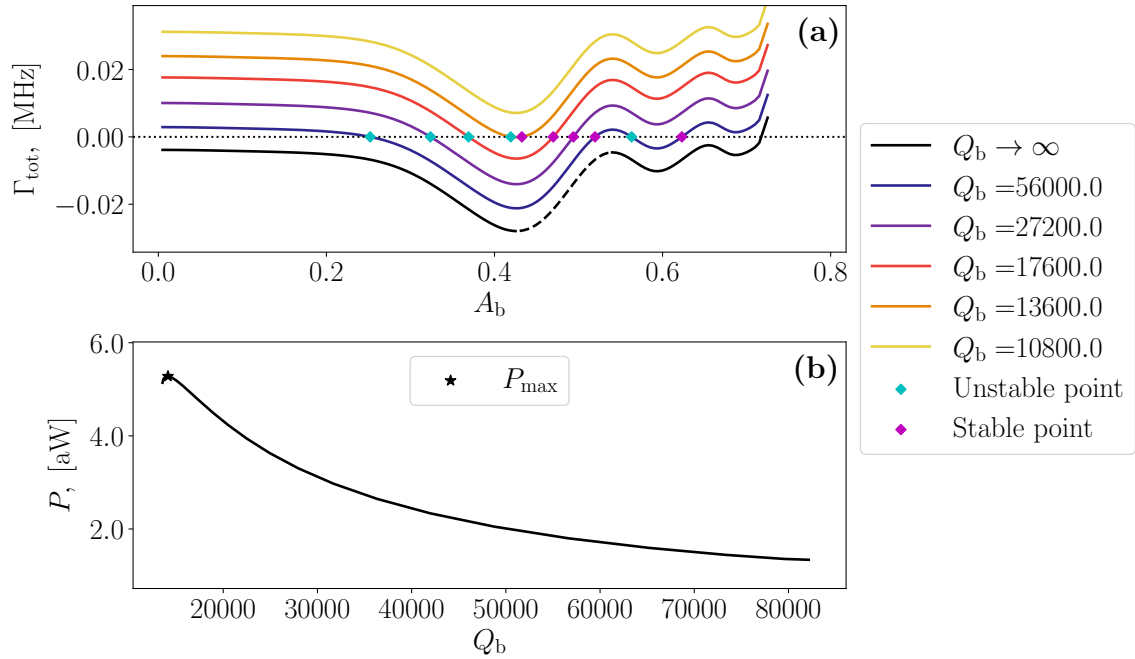


Figure 3: (a) Total dissipation rate $\Gamma_{\text{tot}}(A_b, \theta_b)$ as a function of field amplitude A_b at different intrinsic quality factors Q_b . The stable and unstable stationary points are marked by the cyan and magenta diamonds, respectively. The dashed line segment on the $Q_b \rightarrow \infty$ curve denotes the region where stable points essentially occur in the primary dissipation valley for some Q_b . (b) Output power as a function of the intrinsic quality factor, corresponding to the dashed line segment in panel (a). The star marks the location of the maximum value of output power. The parameters used for computing the results are found in Table 1.

To study the dynamics further, we use Eq. (24) to analyse how the field amplitude A_b evolves as a function of itself. Although there are multiple minima, referred to as negative-dissipation valleys, present in the curves in Fig. 3(a), we focus on the deepest, most prominent valley, occurring at the lowest amplitudes. We refer to it as the primary dissipation valley. Whenever the total dissipation rate is positive, the time derivative of the field amplitude A_b is negative, resulting in a decreasing amplitude in time. Conversely, when the total dissipation rate becomes negative, the amplitude increases with time. Since the total dissipation rate can be negative only within a finite negative dissipation valley, the amplitude increases until it reaches the point where $\Gamma_{\text{tot}} = 0$. Consequently, we can identify stable points along the curves at the zero crossing, where the slope of the curve is positive. In addition, unstable stationary points exist at the zero crossings, where the slope is negative. Near these points,

the amplitude will either decay to zero or start to increase towards the following stable point. In Fig. 3(a), both the stable and unstable stationary points are marked in the curves that have zero crossings. This is precisely what we aimed to demonstrate: the average noise pressure causing coherent microwave generation arising solely from the internal dynamics of the system driven by thermal noise. Only the initial amplitude needs to be prepared by an external agent.

4.1.1 Power and efficiency

In order to estimate the output power of the device, let us assume that the internal losses of resonator B are negligible. This is reasonable, since, as mentioned above, the intrinsic quality factors considered here are much lower than the internal quality factors of the state-of-the-art resonators in circuit quantum electrodynamics (cQED) [65–69]. Consequently, resonator B loses energy at a relative rate γ_b to an external channel, for instance, a transmission line coupled to the resonator. Utilizing this out-flowing energy as the power output of the engine, we define the output power as

$$P = \gamma_b E_b = 2\gamma_b A_b^2 \frac{(1 - N_L)\Phi_0^2}{\pi^2 L_b}, \quad (28)$$

where E_b is the energy stored in resonator B. Based on this, we can compute the attainable output power for all possible stable points by finding the pairs of intrinsic quality factors Q_b and field amplitudes A_b that satisfy the condition $\Gamma_{\text{tot}} = 0$ and $\partial_{A_b} \Gamma_{\text{tot}} > 0$. This is demonstrated in Figs. 3(a),(b), where panel (b) shows the power as a function of Q_b , determined in the range of possible stable points in the primary dissipation valley, depicted in panel (a). Note that because of the A_b^2 -dependence of power, the parameters yielding maximal power output may slightly differ from those yielding the deepest primary dissipation valley.

The efficiency of a heat engine is typically defined as the ratio of the work output per cycle to the heat absorbed from the hot heat bath per cycle. This definition assumes that heat transfer occurs solely through the working fluid, meaning that the hot and cold environments are completely decoupled except for their interactions with the working fluid. However, this assumption does not hold for the present device. Although weak compared to other interactions in the system, there is a continuous coupling between the filter resonators. Therefore, in order to obtain a realistic estimate for the efficiency, we must account for the continuous heat flow through the system, and alter the definition of efficiency accordingly. Consequently, we define efficiency as

$$\eta = \frac{P}{|\langle \dot{Q} \rangle|}, \quad (29)$$

where P is the power computed above, and $\langle \dot{Q} \rangle$ is the average heat flow through the device. Since the non-linear interaction with resonator B is assumed to be a weak perturbation to the linear part of the system, we assume that the heat flow remains largely unaffected by the modulation due to Resonator B. Therefore, we estimate the average heat flow based on a linear system, neglecting Resonator B and treating the combined system of Resonator A and the SQUID loop as a single resonator with the frequency $\omega'_a = 1/\sqrt{C_{\Sigma a}(L_a + L_J/2)}$ and an associated field ϕ'_a . The average heat flow is given by

$$\langle \dot{Q} \rangle = \sum_{f \in [h,c]} \frac{\alpha_{fa}}{\alpha_f} \left(\langle \xi_f(t) \dot{\phi}_f \rangle - 2\gamma_f \langle \dot{\phi}_f^2 \rangle \right), \quad (30)$$

which can be evaluated using similar methods as above. This result and the method for evaluating it are presented in Appendix E.

We find the efficiency of our QHE to reside in the below 1% range, as shown below. This means that over 99% of the heat just flows straight through the device into the cold reservoir. We additionally test the effect of varying the frequency ω'_a , and find that it barely affects the estimated efficiency. These observations validate our method of estimating the efficiency. For completeness, we denote the value of $\eta_C = 1 - T_c/T_h \approx 97\%$ for the Carnot efficiency based on the temperatures listed in Table 1. Additionally, depending on the field amplitude A_b , we find the Otto efficiency to reside in the range $\eta_O = 1 - \omega'_{a,\min}/\omega'_{a,\max} \in [10\%, 50\%]$, where $\omega'_{a,\min}$ and $\omega'_{a,\max}$ are the minimum and maximum values of the effective working fluid angular frequency over the cycle, respectively. (See Sec. 4.4.) We find that the efficiency of our device is significantly lower than either of these theoretical bounds. In principle, the efficiency can be improved by fine-tuning the parameters of the circuit, such as coupling between the filters and resonator A to facilitate heat exchange, filter frequency separation, and frequency of the slow resonator. In this work, however, we merely demonstrate a proof-of-principle possibility of autonomous QHE operation with experimentally feasibly observable output power.

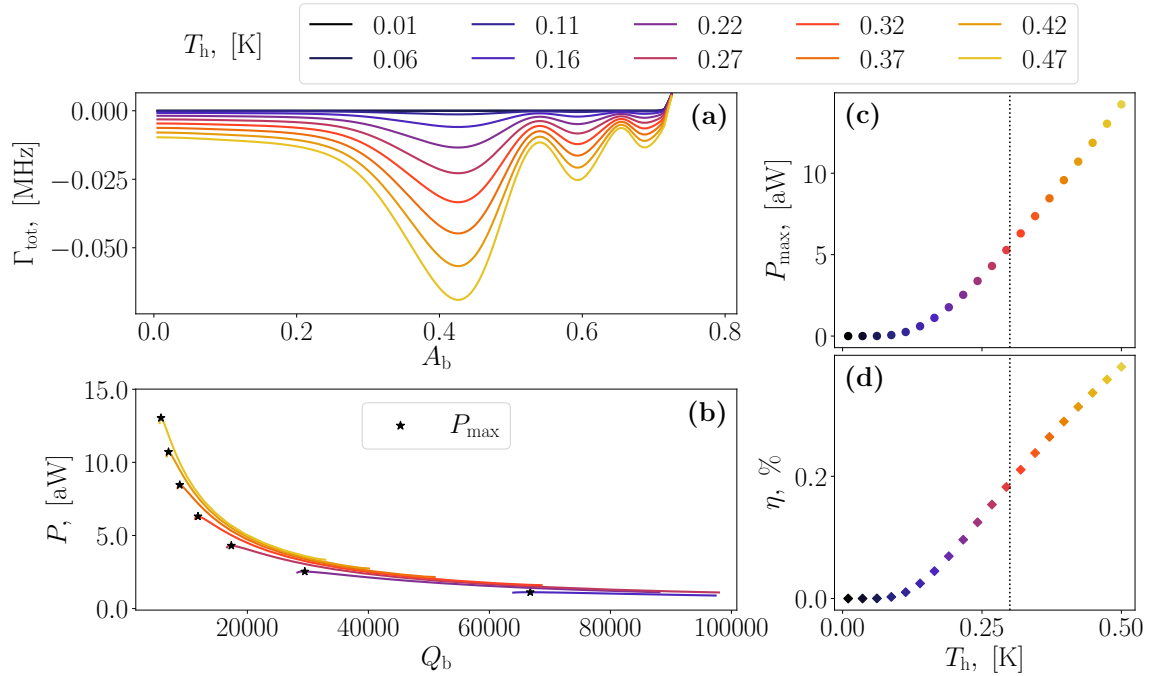


Figure 4: (a) Total dissipation rate $\Gamma_{\text{tot}}(A_b, \theta_b)$ as a function of the field amplitude A_b at various indicated hot-bath temperatures T_h and for an intrinsic dissipation rate of $\gamma_b = 0$. (b) Output power as a function of Q_b , determined from the stable points of the primary dissipation valley. The black stars mark the maximum values. Note that the three lowest-temperature curves are cut out because we limit Q_b to 100000. (c) Maximum attainable output power as a function of T_h . (d) Efficiency corresponding to the data in panel (c). The dotted vertical lines in panels (c) and (d) mark the value of T_h given in Table 1. In panels (a) and (b), we only show every other curve, as compared with the markers in panels (c) and (d), for the sake of clarity. The values in the legend are in units of kelvin, and the parameters used for computing these results and not given here are found in Table 1.

4.2 Parameter sweeps

In addition to showing that the device can reach a stable operation point where coherent power generation occurs, it is insightful to analyse the dependence of the output power on

the parameters of the circuit. Let us study this by carrying out parameter sweeps, keeping all other parameters at fixed values, given in Table 1, while varying one parameter at a time.

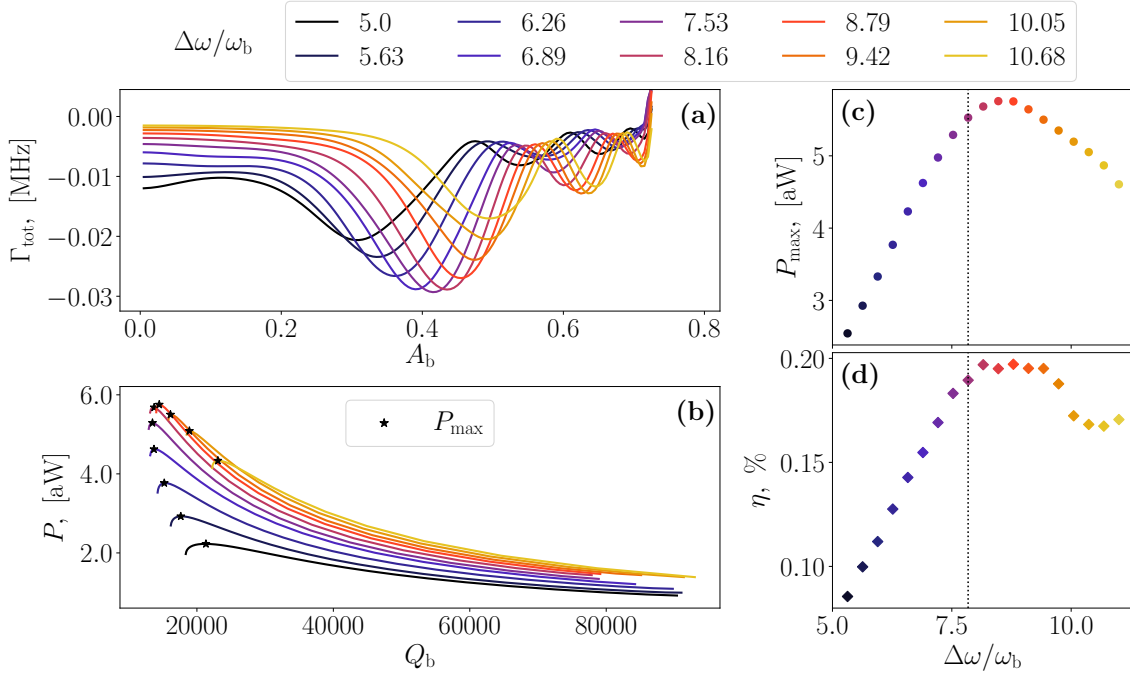


Figure 5: (a) Total dissipation rate $\Gamma_{\text{tot}}(A_b, \theta_b)$ as a function of field amplitude A_b at various filter resonator frequency differences $\Delta\omega = \omega_h - \omega_c$ as indicated and for an intrinsic dissipation rate of $\gamma_b = 0$. (b) Output power as a function of Q_b , determined from the possible stable points of the primary dissipation valley. (c) Maximum attainable output power as a function of $\Delta\omega$. (d) Efficiency corresponding to the data in panel (c). The dotted vertical lines in panels (c) and (d) mark the value of $\Delta\omega$ obtained from the values of filter frequencies, given in Table 1. In panels (a) and (b), we only plot every other curve, as compared to the markers in panels (c) and (d) for the sake of clarity. The parameters used for computing these results that are not given here are found in Table 1.

Perhaps the most fundamental parameter to vary is the temperature of the hot heat bath. In Fig. 4 we present total dissipation, power, and efficiency at different hot bath temperatures. In panel (a), we show the total dissipation rate with $\gamma_b = 0$ as a function of the field amplitude at different hot reservoir temperatures while keeping the cold reservoir at $T_c = 10$ mK. We immediately observe that the primary dissipation valley deforms as a function of the hot-bath temperature. Specifically, it deepens with rising temperature T_h . Consequently, the power output of the device increases monotonically with increasing temperature, as visible in panel (b), where we show the output power as a function of Q_b . The data in panel (b) also show that the output power decreases exponentially as a function of the quality factor Q_b . In panel (c), we display the maxima of output power as a function of T_h . These data further show that the power of the device increases monotonically with increasing temperature. We also observe that as the hot-bath temperature approaches the cold-bath temperature, the work output abates exponentially towards zero, which is an expected consequence of the quantum noise. Lastly, in panel (d) we display the efficiency as a function of the hot-bath temperature. We note that it closely follows the trend of the maximum power in panel (c), but starts to become less steep at high temperatures, in agreement with a finite maximum efficiency.

Two parameters that greatly affect the performance of the heat engine are the centre fre-

quencies of the filters, and especially, the frequency difference $\Delta\omega = \omega_h - \omega_c$. In Fig. 5, we present total dissipation, power, and efficiency at different frequency differences $\Delta\omega$. Panel (a) displays the total dissipation rate with $\gamma_b = 0$ as a function of field amplitude. From here, we observe that increasing the frequency difference deforms the primary dissipation valley and moves the position of the minimum higher in A_b . We find that there exists an optimal frequency difference $\Delta\omega$ that gives the highest negative dissipation rate. This is translated into the attainable output power, as is visible in panel (b), where we show the output power as a function of Q_b . It turns out that there exists an optimal value for the frequency separation $\Delta\omega$, as evidenced by the data in panel (b). This is even more evident from the data in panel (c), where we display the maximum output power as a function of $\Delta\omega$. One may naively think that increasing $\Delta\omega$ would always lead to an equilibrium with higher field amplitude A_b , thus translating into increasing output power as a function of $\Delta\omega$ [45]. This is not the case here, however. Rather, the optimal value seems to be very close to $\Delta\omega = 8.6 \times \omega_b$, and the output power falls off in both directions from here. The assumption that increasing $\Delta\omega$ increases the field amplitude A_b required to reach a steady state is correct though, as visible in panel (a). However, the depth of the dissipation valley diminishes with increasing $\Delta\omega$ and hence causes the feasible γ_b and the energy generation rate to decrease. Regarding the frequency difference, we also note that the chosen value is not optimal, as evinced by the vertical dotted line.

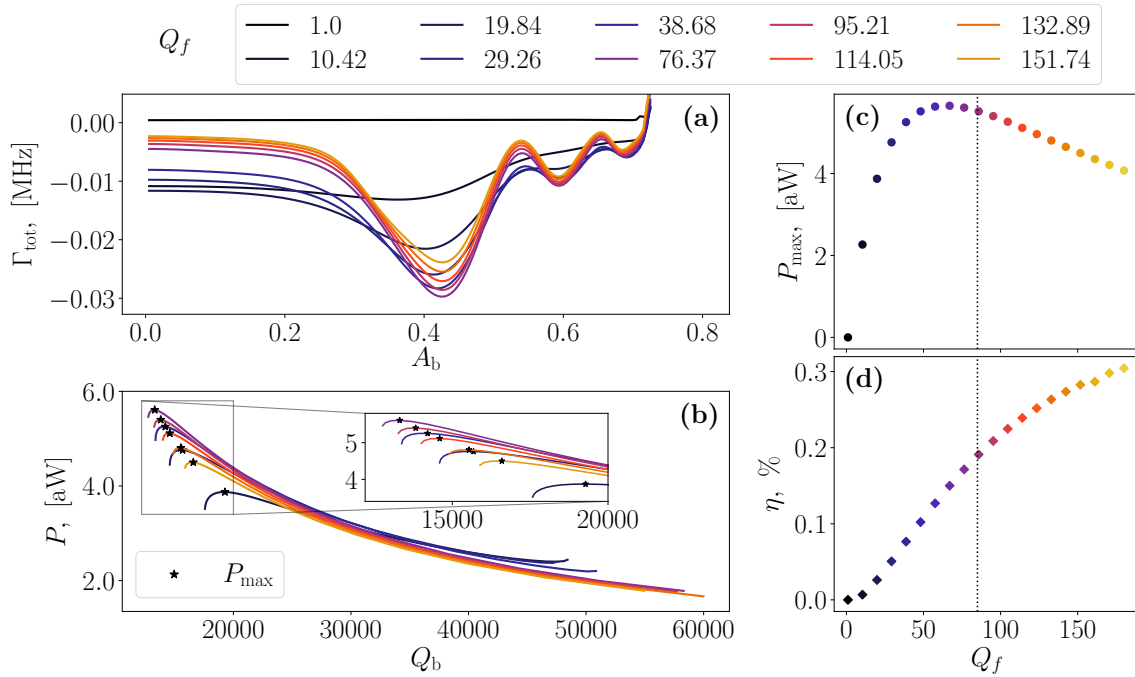


Figure 6: (a) Total dissipation rate $\Gamma_{\text{tot}}(A_b, \theta_b)$ as a function of field amplitude A_b at various indicated filter resonator quality factors $Q_f = \omega_f / \gamma_f$ for an intrinsic dissipation rate of $\gamma_b = 0$. We use the quality factor Q_f for both filters. (b) Output power as a function of Q_b , determined from the possible stable points of the primary dissipation valley. Note that the curve with $Q_f = 1$ in panel (a) does not produce power output. (c) Maximum attainable output power as a function of Q_f . (d) Efficiency corresponding to the data in panel (c). The dotted vertical lines in panels (c) and (d) mark the value of Q_f obtained, given in Table 1. In panels (a) and (b), we only plot every other curve, as compared to the markers in panels (c) and (d) for the sake of clarity. The parameters used for computing these results that are not given here are found in Table 1.

In Fig. 5(d) we display the efficiency as a function of the frequency difference. We observe that below the optimal value, it closely follows the trend of the maximum power in panel (c), but starts to deviate at higher $\Delta\omega$.

To demonstrate the effects of the peaked spectral shape of the filters and the non-Markovian properties of the heat baths, in Fig. 6, we vary the quality factor of the filters, defined as $Q_f = \omega_f/\gamma_f$, which is inversely proportional to the filter linewidth. Here, we use an equal quality factor Q_f for both filters. From panel (a), we find the total dissipation rate Γ_{tot} as a function of the field amplitude A_b , while panel (b) shows the attainable output power as a function of Q_b . From these data, we clearly see that as the spectrum flattens in the limit $Q_f \rightarrow 0$, the negative-dissipation valleys, and therefore the power output, disappear. Although even a modest quality factor Q_f is sufficient to enable power generation, it is evident that the device demands peaked filter spectral shapes in order to function as a quantum heat engine. The peaked spectra effectively provide the mechanism for modulating the coupling of the working fluid to the heat bath over the cycle, as the frequency of the working fluid is modulated. This is a necessary requirement for realizing an Otto cycle [60]. These conclusions are further illustrated in panel (c), where we plot the maximum output power as a function of Q_b . Here we observe a quick increase in power as the filter spectrum becomes narrower. The data in panel (c) further demonstrates that increasing the filter quality factor too much starts to reduce the output power. This is expected, as a higher Q_f translates to weaker coupling to the thermal noise. Finally, in panel (d) we display the efficiency as a function of the filter quality factor Q_f . Below the maximum power, the efficiency enhances with increasing Q_f , as the output power rises. When the output power starts to diminish, the slope of the efficiency also starts to abate. The above observations confirm that the peaked spectral shape of the filters plays an important role in the dynamics of the device, suggesting that non-Markovian effects should not be neglected.

4.3 Quantum disadvantage

Let us revisit the temperature dependence of the hot heat bath. Above, we alluded that the threshold temperature for microwave generation should be a consequence of the quantum noise. In order to highlight the quantum nature of the device, and to investigate the implications of quantum thermal noise to the system, we repeat the computation done for Fig. 4 using the corresponding power spectral density of classical thermal noise. It is obtained from the approximation valid at the high-temperature limit of the quantum version:

$$S_f^{\text{clas}}(\omega) = 8\gamma_f^2 R_f k_B T_f \approx 4\hbar\omega\gamma_f^2 R_f \coth\left(\frac{\hbar\omega}{2k_B T_f}\right), \text{ for } \frac{\hbar\omega}{k_B T_f} \ll 1. \quad (31)$$

This is the only change as compared with how the results in Fig. 4 are obtained.

In Fig. 7, we show the results of the above-defined computation at various hot-bath temperatures. In panel (a), we show the total dissipation rate $\Gamma_{\text{tot}}(A_b, \theta_b)$ as a function of the field amplitude A_b while panel (b) depicts the output power as a function of the intrinsic quality factor Q_b . The results in these panels look qualitatively similar to those in Figs. 4(a) and (b), only with higher negative dissipation and output power. In panel (c), however, we show the maximum output power as a function of T_h , from where we observe that the initial plateau of exponentially vanishing output power, which we observed in Fig. 4(c), has disappeared. In the case of classical noise, the maximum power increases linearly with T_h everywhere. This behaviour is different from the quantum case, and can be explained by the linear temperature dependence of the classical noise spectrum, given by Eq. (31). We observe the corresponding qualitative difference in the efficiency, shown in panel (d). The decrease of the slope of efficiency as temperature rises is slightly more prominent here than in the quantum case. To

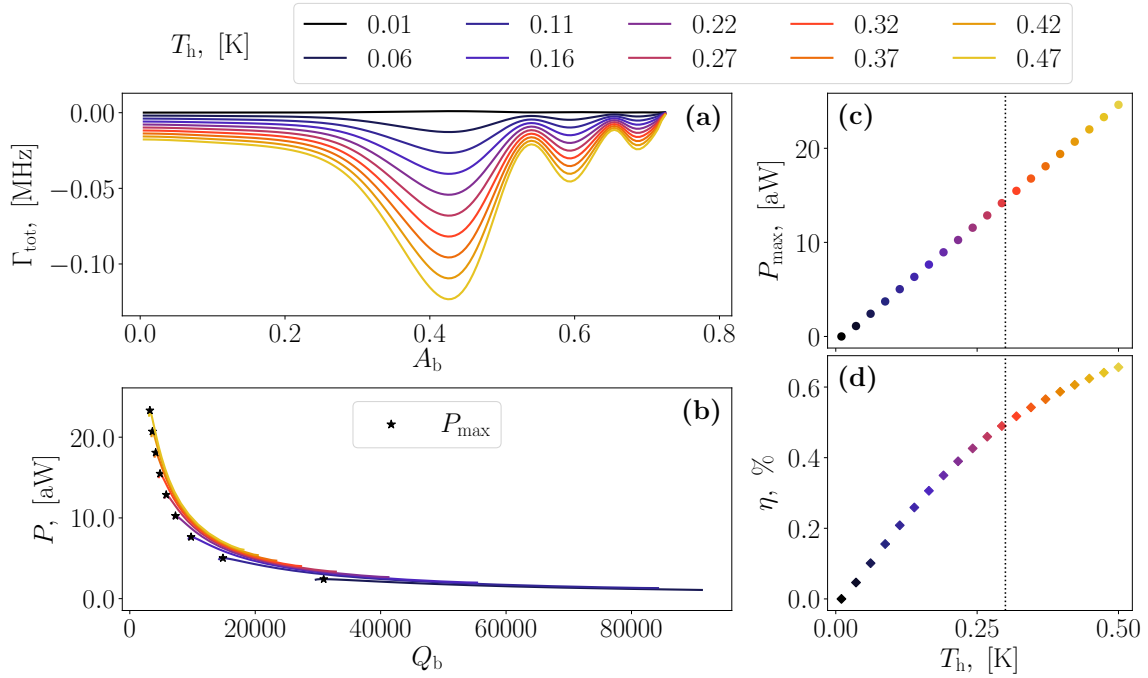


Figure 7: Results in Fig. 4 reproduced using classical noise, characterised by Eq. (31). (a) Total dissipation rate $\Gamma_{\text{tot}}(A_b, \theta_b)$ as a function of field amplitude A_b at various hot bath temperatures T_h . (b) Output power as a function of intrinsic quality factor as determined from the possible stable points of the primary dissipation valley. (c) Maximum attainable output power as a function of T_h . (d) Efficiency corresponding to the data in panel (c). The vertical dotted line in panels (c) and (d) marks the value of T_h given in Table 1. In panels (a) and (b), we only plot every other curve, as compared to the markers in panels (c) and (d) for the sake of clarity. The values in the legend are in units of kelvin, and the fixed parameters used for computing these results are found in Table 1.

conclude, we stress that the temperature of the hot reservoir is much lower than that required for the classical limit to be accurate, as evinced by the ratio $\hbar\omega_h/(k_B T_h) \approx 1.7$. Therefore, the thermal baths here need to be described by quantum noise.

4.4 Comparison to the Otto cycle

Now that we have shown that the device can reach a stable state where power generation is possible, let us analyse the cyclic properties of the device and compare them with the Otto cycle. We study the time-evolution of the working fluid by examining the expectation value $\langle \phi_s^2 \rangle_\xi(t)$, given by Eq. (D.6), as a function of time in Fig. 8(a) at various field amplitudes A_b in the range where stable points generally occur with the parameters given in Table 1. As a first observation, we note that the expectation value oscillates roughly sinusoidally, which matches our expectations and phenomenological understanding [45]. In Fig. 8(b), we show the effective frequency of the working fluid ω'_a , defined in Sec. 3.1.1, as a function of time. We observe that the modulation of the frequency matches the oscillations of the expectation value $\langle \phi_s^2 \rangle_\xi(t)$ up to a small phase shift. This perfectly corroborates our understanding of the dynamics and the above conclusions. Both of the curves in panels (a) and (b) begin to deform with large field amplitudes, which is not surprising, considering that there is some asymmetry in the filter frequencies and couplings.

Figure 8(c) we shown the asymmetry of the rising and falling sections of the expectation

value in Fig. 8(a). The asymmetry is defined as the relative difference between the rising and falling sections of the curve, given by

$$\mathcal{A}(t) = \frac{\langle \phi_s^2 \rangle_\xi(t) - \langle \phi_s^2 \rangle_\xi(-t + \vartheta_0)}{\langle \phi_s^2 \rangle_\xi(t)}, \quad (32)$$

where ϑ_0 is the small phase offset observed in panel (a). We note that in addition to the asymmetry between the maxima and minima of $\langle \phi_s^2 \rangle_\xi(t)$ curve, the oscillation of the expectation value is also slightly asymmetric in time. This suggests that, in terms of the heat engine terminology, the compression and decompression stages of the working fluid slightly differ, which is expected.

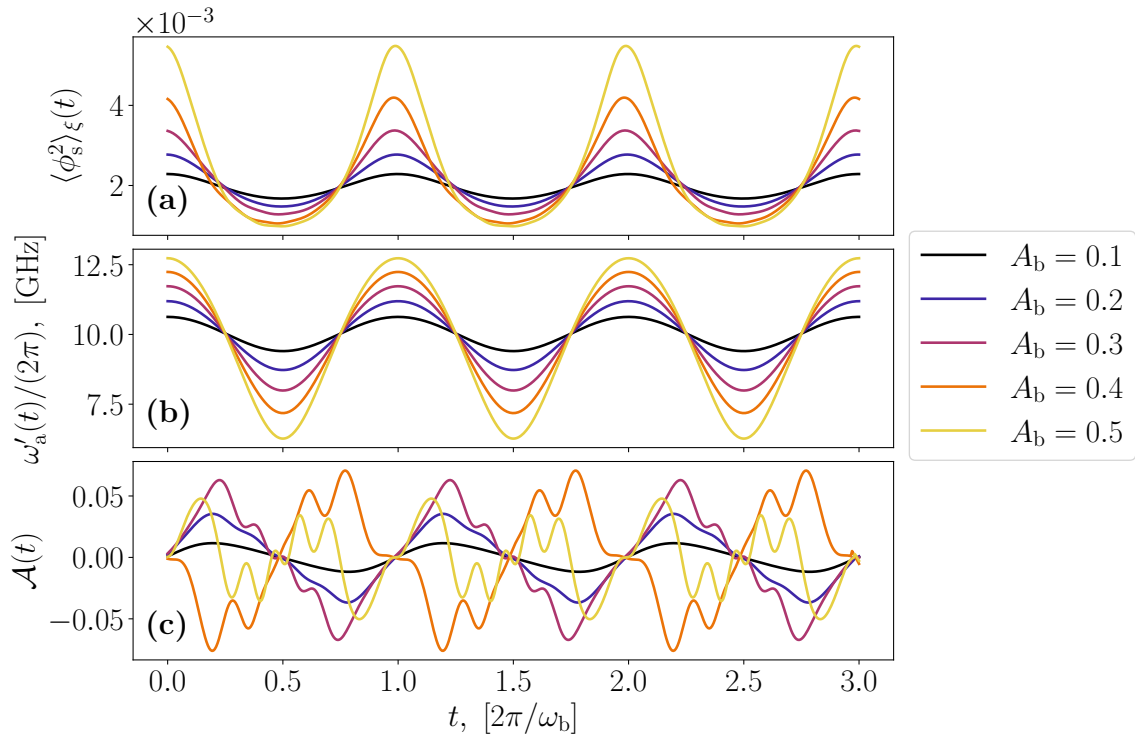


Figure 8: Temporal evolution of the (a) noise expectation value of the square of the effective working fluid field $\langle \phi_s^2 \rangle_\xi(t)$, (b) effective frequency of the working fluid ω'_a , and (c) asymmetry $\mathcal{A}(t)$ of the expectation value $\langle \phi_s^2 \rangle_\xi$ at various steady state field amplitudes A_b . All of these are defined in the main text. The parameters used for computing the results are found in Table 1.

Although in the externally driven quantum Otto heat cycle, the frequency of the working fluid is ideally square-modulated, it seems reasonable to conclude based on this analysis that the working fluid of our system, i.e. resonator A, indeed undergoes an approximate cosine-modulated Otto cycle.

5 Conclusions

We proposed and theoretically analysed an experimentally feasible superconducting quantum circuit capable of realizing an autonomous quantum heat engine based on internal Otto cycles. To validate the operation of the device, we developed an efficient quasiclassical non-Markovian

model to show that the circuit can generate a coherent microwave tone arising purely from heat flow and non-linear internal dynamics. The model enables us to estimate the coherent microwave power generation rate and the efficiency of the device.

We carried out multiple parameter sweeps to demonstrate the effects of the parameters on the dynamics of the device and found the results to be physically sound. Furthermore, we characterized the cyclic evolution of the working fluid in our device, showing that it realizes a sinusoidally driven Otto cycle. Our findings show that the microwave generation rate can be relatively high—well within the observable range in circuit quantum electrodynamics—highlighting the feasibility of an experimental realization.

For the experimental observation of the output power, let us consider the ultrasensitive bolometer of Ref. [24] with the noise in its readout signal of $30 \text{ zW}/\sqrt{\text{Hz}}$ in units of the absorbed power and a thermal time constant of 500 ns. These performance metrics yield roughly a $5 \mu\text{s}$ of integration time to arrive at a signal-to-noise ratio of unity for the 10 aW output power predicted for the heat engine in Fig. 4. Consequently, channelling the microwaves generated by the quantum heat engine to the bolometer input and observing the bolometer response in time is expected to yield a conveniently fast observation of the generated power directly from the heat it deposits on the bolometer. The coherence of the radiation can be unveiled by a homodyne method at low temperatures before the bolometer [70].

Unlike many theoretical works, we analyse an accurately defined physical device, an electric circuit, and explicitly connect the theoretical model to its circuit parameters. The parameters were chosen such that they ensure experimental feasibility with modern fabrication techniques [59, 65, 69, 71], making this work a solid stepping stone toward autonomous thermal machines in cQED. Given the advancements in thermal devices and quantum thermodynamics within superconducting circuits [30, 31, 39–43, 72], the realization of our proposed quantum heat engine appears to be likely in the near future. For high-power operation, exploring engineered environments [44, 73–75], which have recently been shown to enable rapid thermal-state preparation [76], is an interesting direction for future research.

We found the output power of the quantum heat engine to increase monotonically with the temperature of the hot reservoir, providing prospects for potential applications. We also compared the performance of the device when driven by classical noise instead of quantum noise and observed a significant increase in the output power in the classical case. This observation is attributed to the exponential suppression of thermal excitations in low-temperature heat reservoirs as compared with the linear dependence in the classical case. Our findings may provide insights into the limits and effects of low-temperature thermal environments governed by quantum mechanics, as opposed to classically described thermal baths. In any case, our results pave the way for practical thermal machines in cQED, operating at cryogenic temperatures. For instance, the proposed device may possibly serve as a coherent microwave photon source, harnessing thermal energy from temperature differences within a cryostat. In addition to power, we determine the efficiency of the device and find that it resides in the below 1% range. This is due to the weak, but continuous, coupling between the heat baths, which results in over 99% of the heat simply flowing through the device without contributing to power generation. The efficiency of the device is thus significantly below the Carnot and Otto limits of efficiency.

Even though our quasiclassical approach may lead to some missed quantum character, we prioritized retaining the non-linearity and non-Markovianity of the system as the key points of methodological novelty. Although a fully quantum analysis will undoubtedly introduce corrections to our quasiclassical estimates, we do not expect it to eliminate the underlying phenomenon. Investigating the complete quantum nature of the device remains a topic for future work, but the results presented here serve as a significant and compelling proof of concept.

Beyond quantization, another promising theoretical future direction is to extend the analysis of the non-linear coupling to a higher order. On the experimental side, it would be fruitful to explore various realizations of the proposed quantum heat engine and compare their respective advantages and limitations. Finally, we point out that the presented approach does not directly provide an estimate of work fluctuations; however, it should not be overlooked that phase and amplitude fluctuations in ϕ_b are inherently present. Understanding and mitigating these fluctuations in the coherent output field of the heat engine calls for further studies.

Acknowledgements

We acknowledge the support from the members of the QCD and PICO groups at Aalto University. Especially, we thank J. Pekola, B. Karimi, C. Satrya, M. Tuokkola, T. Mörstedt, J. Ma, H. Kivijärvi, H. Suominen, M. Gunyho, Y. Sunada, Q. Chen, and A. Keränen for fruitful scientific discourse and other help.

Funding information This work was funded by the Academy of Finland Centre of Excellence program (Projects No. 352925 and No. 336810) and Academy of Finland Grants No. 316619 and No. 349594 (THEPOW). We also acknowledge funding from the European Research Council under Advanced Grant No. 101053801 (ConceptQ), and Business Finland under the Quantum Technologies Industrial (QuTI) project (Grant No. 128291).

A Deriving the optomechanical approximation

To handle the trigonometric potential in the SQUID Lagrangian (2), let us derive an approximation for it. Before expanding the trigonometric functions, however, let us analyse the potential energy related to the inductances in the SQUID loop. The potential energy is given as

$$U = \frac{(\varphi_g - \Phi_{\text{ext}})^2}{2L_g} - E_J \cos\left(\frac{2\pi\varphi_s}{\Phi_0}\right) - E_J \cos\left(\frac{2\pi}{\Phi_0}[\varphi_s - \varphi_g]\right), \quad (\text{A.1})$$

where we have chosen to rewrite the external flux, Φ_{ext} , outside of the cosine, as can be done. Let us now find the potential minimum with respect to the fields φ_s and φ_g . By applying $\partial U / \partial \varphi_s = 0$ and $\partial U / \partial \varphi_g = 0$, we find two conditions, the first simply being $\varphi_s^{(0)} = \varphi_g^{(0)} / 2$, and the second stating

$$\frac{\varphi_g^{(0)} - \Phi_{\text{ext}}}{L_g} + \frac{2E_J\pi}{\Phi_0} \sin\left(\frac{\pi}{\Phi_0}\varphi_g^{(0)}\right) = 0. \quad (\text{A.2})$$

This is a transcendental equation that needs to be solved numerically. This does not matter as we will resort to numerics at the end anyhow.

Let us now assume a solution, $\varphi_g^{(0)}$, of the above equation. We apply a change of variable to the fields inductively coupled to the SQUID in order to shift the fields close to the potential minimum. We define new field variables as

$$\tilde{\varphi}_a = \varphi_a - \varphi_g^{(0)} / 2, \quad \tilde{\varphi}_s = \varphi_s - \varphi_g^{(0)} / 2, \quad (\text{A.3})$$

$$\tilde{\varphi}_b = \varphi_b - \varphi_g^{(0)} / 2, \quad \tilde{\varphi}_g = \varphi_g - \varphi_g^{(0)} / 2. \quad (\text{A.4})$$

Applying this to the SQUID Lagrangian, one obtains

$$\begin{aligned}\mathcal{L}_S &= -\frac{(\tilde{\varphi}_g + \varphi_g^{(0)} - \Phi_{\text{ext}})^2}{2L_g} + E_J \cos\left(\frac{2\pi}{\Phi_0} [\tilde{\varphi}_s + \varphi_g^{(0)}/2]\right) + E_J \cos\left(\frac{2\pi}{\Phi_0} [\tilde{\varphi}_s - \tilde{\varphi}_g - \varphi_g^{(0)}/2]\right) \\ &= -\frac{(\tilde{\varphi}_g + \varphi_g^{(0)} - \Phi_{\text{ext}})^2}{2L_g} + 2E_J \cos\left(\frac{\pi}{\Phi_0} [\tilde{\varphi}_g + \varphi_g^{(0)}]\right) \cos\left(\frac{\pi}{\Phi_0} [2\tilde{\varphi}_s - \tilde{\varphi}_g]\right).\end{aligned}\quad (\text{A.5})$$

Upon expanding the trigonometric functions with respect to $\tilde{\varphi}_g$ and $\tilde{\varphi}_s$, we obtain

$$\begin{aligned}\cos\left(\frac{\pi}{\Phi_0} [\tilde{\varphi}_g + \varphi_g^{(0)}]\right) \cos\left(\frac{\pi}{\Phi_0} [2\tilde{\varphi}_s - \tilde{\varphi}_g]\right) &= \left[\cos\left(\frac{\pi}{\Phi_0} \varphi_g^{(0)}\right) - \frac{\pi}{\Phi_0} \sin\left(\frac{\pi}{\Phi_0} \varphi_g^{(0)}\right) \tilde{\varphi}_g + \dots \right] \\ &\times \left\{ \left[1 - \frac{2\pi^2}{\Phi_0^2} \tilde{\varphi}_s^2 + \dots \right] \left[1 - \frac{\pi^2}{2\Phi_0^2} \tilde{\varphi}_g^2 + \dots \right] + \frac{2\pi^2}{\Phi_0^2} \tilde{\varphi}_s \tilde{\varphi}_g + \dots \right\}.\end{aligned}\quad (\text{A.6})$$

Next, we multiply open the parentheses, truncate the expression to second order in field variables everywhere, and plug the result back into the Lagrangian. As we do this, we discover the left-hand side of Eq. (A.2) multiplied by $\tilde{\varphi}_g$ appearing in the Lagrangian. As this must be zero, we can safely drop it. Further, we will drop all constants, as they will not affect the equations of motion anyhow. The Lagrangian now reads

$$\begin{aligned}\mathcal{L}_S &= 2E_J \left[-\frac{\pi^2}{\Phi_0^2} \cos\left(\frac{\pi}{\Phi_0} \varphi_g^{(0)}\right) \tilde{\varphi}_g^2 - \frac{2\pi^2}{\Phi_0^2} \cos\left(\frac{\pi}{\Phi_0} \varphi_g^{(0)}\right) \tilde{\varphi}_s^2 + \frac{2\pi^3}{\Phi_0^3} \sin\left(\frac{\pi}{\Phi_0} \varphi_g^{(0)}\right) \tilde{\varphi}_g \tilde{\varphi}_s^2 \right. \\ &\quad \left. + \frac{2\pi^2}{\Phi_0^2} \cos\left(\frac{\pi}{\Phi_0} \varphi_g^{(0)}\right) \tilde{\varphi}_g \tilde{\varphi}_s - \frac{2\pi^3}{\Phi_0^3} \sin\left(\frac{\pi}{\Phi_0} \varphi_g^{(0)}\right) \tilde{\varphi}_g^2 \tilde{\varphi}_s \right] - \frac{\tilde{\varphi}_g^2}{2L_g},\end{aligned}\quad (\text{A.7})$$

Above, the first two terms in the brackets give inductive energy terms arising from the SQUID inductance. The third term is the optomechanical coupling, while the fourth and fifth terms are the linear and inverse optomechanical couplings. As a final step, we will drop the linear interaction term as well as the inverse optomechanical coupling, as they are assumed weak due to the large frequency offset between the modes $\tilde{\varphi}_g$ and $\tilde{\varphi}_s$. This yields the approximated Lagrangian given by Eq. (4).

B Simplification of the equations of motion

As explained in the main text, our goal is to integrate out the field degrees of freedom $\tilde{\varphi}_a$, $\tilde{\varphi}_f$ and $\tilde{\varphi}_g$. We begin by solving $\tilde{\varphi}_g$ from Eq. (7d) in the time domain, which requires nothing but standard algebra. This solution is then inserted into the Eqs. (7b) and (7c), where the resulting third-order term ($\sim \tilde{\varphi}_s^3$) is neglected, in accordance with the truncation of the series discussed in Appendix A. We thus eliminate $\tilde{\varphi}_g$, leaving us with four equations. The resulting form of Eq. (7c), governing the evolution of $\tilde{\varphi}_b$, readily matches the final shape of Eq. (10) in the main text. Consequently, we only need to combine the three remaining equations.

In order to derive Eq. (9) in the main text, we need to eliminate $\tilde{\varphi}_f$ and $\tilde{\varphi}_a$. First, we solve Eq. (7e) for $\tilde{\varphi}_f$ via Fourier transform, yielding

$$\hat{\tilde{\varphi}}_f = \frac{\xi_f(\omega) + \alpha_f \omega^2 \hat{\tilde{\varphi}}_a}{\omega_f^2 - \omega^2 - 2i\gamma_f \omega}.\quad (\text{B.1})$$

We additionally Fourier transform Eq. (7a), and substitute the above solution in there, resulting in

$$-\omega^2 \hat{\varphi}_a + \omega_a^2 (\hat{\varphi}_a - \hat{\varphi}_s) - \omega^2 \sum_f \alpha_f \wp_f(\omega) \hat{\varphi}_a = \sum_f \wp_f(\omega) \xi_f(\omega), \quad (\text{B.2})$$

where we utilize the helper function $\wp_f(\omega)$, defined in the main text by Eq. (14). The above equation solves to

$$\hat{\varphi}_a = \frac{\omega_a^2 \hat{\varphi}_s + \sum_f \wp_f(\omega) \xi_f(\omega)}{\omega_a^2 - \omega^2 \left[1 + \sum_f \alpha_f \wp_f(\omega) \right]}. \quad (\text{B.3})$$

We further Fourier transform Eq. (7b) and insert the above solution into the obtained equation, finally yielding

$$[\omega_s^2 - \mathcal{K}(\omega)] \hat{\varphi}_s(\omega) - \frac{2g_0^2}{C_{\Sigma a} N_L} \chi(\omega) = \xi(\omega), \quad (\text{B.4})$$

where $\chi(\omega)$ denotes the Fourier transform of $\tilde{\varphi}_s(t)\tilde{\varphi}_b(t)$, and the angular frequency ω_s , the total memory kernel $\mathcal{K}(\omega)$, and the total noise source function $\xi(\omega)$ are defined in the main text. Fourier transforming the above equation back to the time domain yields an equation of the form Eq. (9) in the main text.

As a final step, we transform the field variables to be dimensionless. To this end, we write the field variable in a form $\tilde{\varphi}_i = \sqrt{\hbar Z_i/2} x_i \phi_i$, where $i = s, b$, Z_i is the characteristic impedance of the resonator, ϕ_i is the dimensionless field variable, and x_i is a dimensional scaling constant. We substitute ϕ_i into the equations derived above, and find x_i such that the units match throughout the equation. We find $x_i = \Phi_0/\pi\sqrt{2/(\hbar Z_i)}$. With this, we finally write down the Eqs. (9) and (10) given in the main text.

C Numerical solution of the Green's function

To derive Eq. (19) in the main text, we first utilize Eq. (17), where we expand the cosine in terms of exponential functions. Next, we use the Fourier transform of the Green's function, given by Eq. (18) in the main text. Simple substitution of these definitions yields

$$\begin{aligned} & \frac{1}{2\pi} \iint_{-\infty}^{\infty} [\omega_s^2 - \mathcal{K}(\omega)] G(\omega, \omega') e^{-i\omega t + i\omega' t'} d\omega d\omega' \\ & + \frac{2g_s^2 A_b}{2\pi} \iint_{-\infty}^{\infty} (e^{-i[(\omega_b + \omega)t + \theta]} + e^{i[(\omega_b - \omega)t + \theta]}) G(\omega, \omega') e^{i\omega' t'} d\omega d\omega' = \delta(t - t'), \end{aligned} \quad (\text{C.1})$$

where we neglect the time-dependence of A_b and θ_b , as explained in the main text. A change variables ($\omega_b \pm \omega \rightarrow \pm\omega$) on the latter row gives

$$\begin{aligned} & \frac{1}{2\pi} \iint_{-\infty}^{\infty} [\omega_s^2 - \mathcal{K}(\omega)] G(\omega, \omega') e^{-i\omega t + i\omega' t'} d\omega d\omega' \\ & + \frac{2g_s^2 A_b}{2\pi} \iint_{-\infty}^{\infty} [G(\omega - \omega_b, \omega') e^{-i\theta} + G(\omega + \omega_b, \omega') e^{i\theta}] e^{-i\omega t + i\omega' t'} d\omega d\omega' = \delta(t - t'). \end{aligned} \quad (\text{C.2})$$

To obtain Eq. (19), we Fourier transform the delta function on the right-hand side and drop the Fourier integrals.

Next, we derive the matrix equation for the Green's function, Eq. (21). Upon inserting the series expansion of the Green's function, given by Eq. (20), into Eq. (19), we obtain

$$\sum_n [P(\omega)G_n + R^*(\theta_b)G_{n-1} + R(\theta_b)G_{n+1}] \delta(\omega - \omega' - n\omega_b) = \delta(\omega - \omega'), \quad (\text{C.3})$$

where we shift the indices of the latter two terms by one to write the terms under the same sum. Taking the integral over ω , one finds the Eq. (21) given in the main text. This set of equations can be written as a matrix equation:

$$\begin{pmatrix} \cdot & \cdot & \cdot & \cdot & \cdot & \cdot \\ \cdot & P(\omega - 2\omega_b) & R(A_b, \theta_b) & 0 & 0 & \cdot \\ \cdot & R^*(A_b, \theta_b) & P(\omega - \omega_b) & R(A_b, \theta_b) & 0 & \cdot \\ \cdot & 0 & R^*(A_b, \theta_b) & P(\omega) & R(A_b, \theta_b) & \cdot \\ \cdot & 0 & 0 & R^*(A_b, \theta_b) & P(\omega + \omega_b) & R(A_b, \theta_b) \\ \cdot & 0 & 0 & 0 & R^*(A_b, \theta_b) & P(\omega + 2\omega_b) \\ \cdot & \cdot & \cdot & \cdot & \cdot & \cdot \end{pmatrix} \begin{pmatrix} \cdot \\ G_{-2} \\ G_{-1} \\ G_0 \\ G_1 \\ G_2 \\ \cdot \end{pmatrix} = \begin{pmatrix} \cdot \\ 0 \\ 0 \\ 1 \\ 0 \\ 0 \\ \cdot \end{pmatrix}. \quad (\text{C.4})$$

Solving this matrix equation numerically is very efficient, since solving a matrix equation with a banded matrix is a linear time operation in n [77], as opposed to inverting an arbitrary matrix, which has cubic time complexity in n .

Once the above matrix equation is solved to the desired degree in n , the Green's function can be expressed through Eq. (20) in the frequency domain. This allows us to solve Eq. (9) for an arbitrary source $\xi(t)$. In general, the solution to a differential equation is given as a convolution of the Green's function with the source:

$$\phi_s(t) = \int_{-\infty}^{\infty} G(t', t) \xi(t') dt'. \quad (\text{C.5})$$

D Noise and time averages

As explained in the main text, we want to compute the noise expectation value of ϕ_s^2 . Starting from the general solution of ϕ_s obtained above, we express this as

$$\langle \phi_s^2 \rangle_{\xi}(t) = \left\langle \int \int_{-\infty}^{\infty} G(t', t) \xi(t') G(t'', t) \xi(t'') dt' dt'' \right\rangle. \quad (\text{D.1})$$

Let us Fourier transform the noise functions and rearrange the expectation value to obtain

$$\langle \phi_s^2 \rangle_{\xi}(t) = \frac{1}{4\pi^2} \int \int \int_{-\infty}^{\infty} G(t', t) G(t'', t) \langle \xi(\omega') \xi(\omega'') \rangle e^{-i\omega' t'} e^{-i\omega'' t''} dt' dt'' d\omega' d\omega''. \quad (\text{D.2})$$

By the properties of the noise function, we know that the expectation value here is given as $\langle \xi_f(\omega) \xi_f(\omega') \rangle = 2\pi \delta(\omega + \omega') S_f(\omega)$, where $S(\omega)$ is the noise spectral density. Upon inserting this in and taking the ω'' integral, the above becomes

$$\langle \phi_s^2 \rangle_{\xi}(t) = \frac{1}{2\pi} \int \int_{-\infty}^{\infty} G(t', t) G(t'', t) S(\omega') e^{-i\omega' t'} e^{i\omega' t''} dt' dt'' d\omega', \quad (\text{D.3})$$

where we use the property $S(-\omega) = S(\omega)$ of the spectral density. Next, we shall insert the Fourier transform of the Green's function given by Eq. (18), yielding

$$\begin{aligned} \langle \phi_s^2 \rangle_\xi(t) = & \left(\frac{1}{2\pi} \right)^3 \int \cdots \int_{-\infty}^{\infty} G(\omega'', \omega) G(\tilde{\omega}, \tilde{\omega}') S(\omega') \\ & \times e^{-i\omega'' t' + i\omega t} e^{-i\tilde{\omega} t'' + i\tilde{\omega}' t} e^{-i\omega' t' + i\omega' t''} dt' dt'' d\omega d\omega' d\omega'' d\tilde{\omega} d\tilde{\omega}'. \end{aligned} \quad (D.4)$$

Here we note that both t' and t'' integrals can be used to yield Dirac delta functions. We first use the t' integral to produce $\delta(\omega' + \omega'')$ and take the ω'' integral immediately. After this, we utilize the t'' integral to produce $\delta(\tilde{\omega} - \omega')$ and take the $\tilde{\omega}$ integral. This finally yields

$$\langle \phi_s^2 \rangle_\xi(t) = \frac{1}{2\pi} \iint_{-\infty}^{\infty} G(-\omega', \omega) G(\omega', \tilde{\omega}') S(\omega') e^{it(\omega + \tilde{\omega}')} d\omega d\omega' d\tilde{\omega}'. \quad (D.5)$$

As a result of the numerical solution of the Green's function, we want to express the above result in terms of the series representation of the Green's function. By direct substitution, we obtain

$$\begin{aligned} \langle \phi_s^2 \rangle_\xi &= \frac{1}{2\pi} \iiint_{-\infty}^{\infty} \sum_{n,m} G_n(-\omega') G_m(\omega') \delta(-\omega' - \omega - n\omega_b) \delta(\omega' - \tilde{\omega}' - m\omega_b) \\ &\quad \times S(\omega') e^{it(\omega + \tilde{\omega}')} d\omega d\omega' d\tilde{\omega}' \\ &= \frac{1}{2\pi} \int_{-\infty}^{\infty} \sum_{n,m} G_n(-\omega') G_m(\omega') S(\omega') e^{-it(n+m)\omega_b} d\omega'. \end{aligned} \quad (D.6)$$

As a final step, let us foresightfully time-average the above expression over one period of oscillation of the mode ϕ_b . Let us consider the Fourier harmonic resonant to the mode, so that the time-average reads

$$\begin{aligned} \langle \phi_s^2 \rangle_{\xi,t} &= \frac{\omega_b}{2\pi} \frac{1}{2\pi} \int_0^{2\pi/\omega_b} e^{i\omega_b t} \int_{-\infty}^{\infty} \sum_{n,m} G_n(-\omega) G_m(\omega) S(\omega) e^{-it(n+m)\omega_b} d\omega dt \\ &= \frac{\omega_b}{2\pi} \frac{1}{2\pi} \int_{-\infty}^{\infty} \sum_{nm} G_n(-\omega) G_m(\omega) S(\omega) \int_0^{2\pi/\omega_b} e^{-it(n+m-1)\omega_b} dt d\omega, \end{aligned} \quad (D.7)$$

where we rearrange the formula such that we obtain the integral expression of the Kronecker delta as given by the time-integral. With this, we simplify the result:

$$\begin{aligned} \langle \phi_s^2 \rangle_{\xi,t}(A_b, \theta_b) &= \frac{1}{2\pi} \int_{-\infty}^{\infty} \sum_{n,m} G_n(-\omega) G_m(\omega) S(\omega) \delta_{m,-n+1} d\omega \\ &= \frac{1}{2\pi} \int_{-\infty}^{\infty} \sum_n G_n(\omega) G_{n-1}^*(\omega) S(\omega) d\omega, \end{aligned} \quad (D.8)$$

where we use $G_{-n}(-\omega) = G_n^*(\omega)$. We now have a function of A_b and θ_b describing the average noise pressure on the mode ϕ_b .

As mentioned in the main text, in order to derive the equations of motion for the amplitude and phase of the mode ϕ_b , we once again use $\phi_b(t) = A_b(t) (e^{-i[\omega_b t + \theta_b(t)]} + e^{i[\omega_b t + \theta_b(t)]})$. The derivatives then read

$$\dot{\theta}_b(t) = \dot{A}_b(t) e^{-i[\omega_b t + \theta_b(t)]} - iA_b(t) [\omega_b + \dot{\theta}_b(t)] e^{-i[\omega_b t + \theta_b(t)]} + c.c., \quad (D.9)$$

$$\begin{aligned} \ddot{\phi}_b(t) &= \ddot{A}_b(t) e^{-i[\omega_b t + \theta_b(t)]} - 2i\dot{A}_b(t) [\omega_b + \dot{\theta}_b(t)] e^{-i[\omega_b t + \theta_b(t)]} \\ &\quad - iA_b(t) \ddot{\theta}_b(t) e^{-i[\omega_b t + \theta_b(t)]} - A_b(t) [\omega_b + \dot{\theta}_b(t)]^2 e^{-i[\omega_b t + \theta_b(t)]} + c.c. \end{aligned} \quad (D.10)$$

In the spirit of the WKB approximation, let us immediately drop the second derivatives, products and powers of derivatives, and the terms $\gamma_b \dot{A}_b$ and $\gamma_b \dot{\theta}_b$. Upon inserting the Fourier component shown above of the remaining expressions into Eq. (23), we obtain

$$[-2i\omega_b \dot{A}_b(t) - 2\omega_b A_b(t) \dot{\theta}_b(t) - 2i\gamma_b A_b \omega_b] e^{-i[\omega_b t + \theta_b(t)]} - g_b^2 \langle \phi_s^2 \rangle_{\xi} (A_b, \theta_b) = 0. \quad (\text{D.11})$$

The reason for computing the time-average above now becomes apparent: multiplying this equation by $e^{i[\omega_b t + \theta_b(t)]}$ and time-averaging over the whole equation gives the exact term computed above multiplied by $e^{i\theta_b(t)}$. Decomposing this result into the real and imaginary parts gives

$$A_b(t) \dot{\theta}_b + \frac{g_b^2}{2\omega_b} \text{Re}[\langle \phi_s^2 \rangle_{\xi, t} (A_b, \theta_b) e^{i\theta_b(t)}] = 0, \quad (\text{D.12})$$

$$\dot{A}_b(t) + \gamma_b A_b + \frac{g_b^2}{2\omega_b} \text{Im}[\langle \phi_s^2 \rangle_{\xi, t} (A_b, \theta_b) e^{i\theta_b(t)}] = 0. \quad (\text{D.13})$$

In the expression given in the main text Eq. (26) the phase exponent $e^{i\theta_b(t)}$ has been included in the definition of $\langle \phi_s^2 \rangle_{\xi, t} (A_b, \theta_b)$.

E Estimating efficiency

As explained in the main text, in order to estimate the efficiency of the device, we need to compute the net heat flow through the system. We start with the following set of equations describing the stationary system, where we ignore resonator B and threat resonator A and the SQUID loop as one tunable frequency resonator with frequency ω'_a and field variable ϕ'_a :

$$\ddot{\phi}'_a + \omega_a'^2 \phi'_a + \sum_{f \in [h, c]} \alpha_{fa} \ddot{\phi}_f = 0, \quad (\text{E.1a})$$

$$\ddot{\phi}_f + \omega_f^2 \phi_f + 2\gamma_f \dot{\phi}_f + \alpha_f \ddot{\phi}'_a = \xi_f(t), \quad (\text{E.1b})$$

In order to compute the derivative of total energy, we multiply the first equation by $\dot{\phi}'_a$ and the latter by $\dot{\phi}_f$. By extracting total time derivatives where possible, we obtain

$$\frac{d}{dt} \left[\frac{\dot{\phi}_a'^2}{2} + \frac{\omega_a'^2}{2} \phi_a'^2 \right] + \sum_{f \in [h, c]} \alpha_{fa} \ddot{\phi}_f \dot{\phi}'_a = 0, \quad (\text{E.2a})$$

$$\frac{\alpha_{fa}}{\alpha_f} \frac{d}{dt} \left[\frac{\dot{\phi}_f^2}{2} + \frac{\omega_f^2}{2} \phi_f^2 \right] + 2\gamma_f \frac{\alpha_{fa}}{\alpha_f} \dot{\phi}_f^2 + \alpha_{fa} \ddot{\phi}'_a \dot{\phi}_f = \frac{\alpha_{fa}}{\alpha_f} \xi_f(t) \dot{\phi}_f, \quad (\text{E.2b})$$

where we also multiply the latter equation by α_{fa}/α_f . Next, we sum together the equations, which yields

$$\frac{d}{dt} \left[\frac{\dot{\phi}_a'^2}{2} + \frac{\omega_a'^2}{2} \phi_a'^2 + \sum_{f \in [h, c]} \frac{\alpha_{fa}}{\alpha_f} \left(\frac{\dot{\phi}_f^2}{2} + \frac{\omega_f^2}{2} \phi_f^2 + \alpha_f \dot{\phi}_f \dot{\phi}_a \right) \right] = \sum_{f \in [h, c]} \frac{\alpha_{fa}}{\alpha_f} (\xi_f(t) \dot{\phi}_f - 2\gamma_f \dot{\phi}_f^2). \quad (\text{E.3})$$

On the left, we identify the time derivative of the total energy of the system. Since all the energy within the system is thermal energy, we can equate this to the derivative of heat, i.e.,

heat flow through the system. Therefore, we have

$$\dot{Q} = \sum_{f \in [h, c]} \frac{\alpha_{fa}}{\alpha_f} \left(\xi_f(t) \dot{\phi}_f - 2\gamma_f \dot{\phi}_f^2 \right). \quad (\text{E.4})$$

The above result is given in terms of the noise function $\xi_f(t)$, and therefore noisy itself. Consequently, we want to estimate the average heat flow, quite similarly to what we did with the field ϕ_s above. In order to proceed, we need to know the field ϕ_f . In the stationary case, it can be solved from the above set of equations (E.1) via Fourier transformation. In Fourier space, we have

$$-\omega^2 \phi'_a + \omega_a'^2 \phi'_a - \omega^2 \sum_{f \in [h, c]} \alpha_{fa} \phi_f = 0, \quad (\text{E.5a})$$

$$-\omega^2 \phi_f + \omega_f^2 \phi_f - 2i\gamma_f \omega \phi_f - \omega^2 \alpha_f \phi'_a = \xi_f(\omega), \quad (\text{E.5b})$$

which can be solved by standard algebra. For the filter degrees of freedom, we obtain

$$\varphi_f(\omega) = \sum_{f' \in [h, c]} G_{ff'}(\omega) \xi_{f'}(\omega), \quad (\text{E.6})$$

with the Green's functions defined as

$$G_{ff}(\omega) = \frac{\mathcal{P}_f(\omega)}{\mathcal{D}(\omega)}, \quad G_{f \neq f'}(\omega) = \frac{\alpha_f \alpha_{f'a} \omega^4}{\mathcal{D}(\omega)}, \quad (\text{E.7})$$

where $f, f' \in [h, c]$, and we define

$$\mathcal{P}_f(\omega) = \vartheta_f(\omega) (\omega_a'^2 - \omega^2) - \alpha_f \alpha_{fa} \omega^4, \quad (\text{E.8})$$

$$\mathcal{D}(\omega) = (\omega_a'^2 - \omega^2) \prod_{f \in [h, c]} \vartheta_f(\omega) - \omega^4 \sum_{f \neq f'} \alpha_f \alpha_{f'a} \vartheta_{f'}(\omega), \quad (\text{E.9})$$

$$\vartheta_f(\omega) = \omega_f^2 - \omega^2 - 2i\omega\gamma_f. \quad (\text{E.10})$$

Though we will continue to work in the Fourier domain, we give the solution to the field degrees of freedom in the time domain for completeness, which reads

$$\varphi_f(t) = \sum_{f' \in [h, c]} \int_{-\infty}^{\infty} G_{ff'}(t - \tau) \xi_{f'}(\tau) d\tau. \quad (\text{E.11})$$

It is now possible to estimate the expectation value

$$\langle \dot{Q} \rangle = \sum_{f \in [h, c]} \frac{\alpha_{fa}}{\alpha_f} \left(\langle \xi_f(t) \dot{\phi}_f \rangle - 2\gamma_f \langle \dot{\phi}_f^2 \rangle \right), \quad (\text{E.12})$$

which we can write via Fourier transform as

$$\begin{aligned} \langle \dot{Q} \rangle = \sum_{f \in [h, c]} \frac{\alpha_{fa}}{\alpha_f} & \left(\frac{1}{4i\pi^2} \iint_{-\infty}^{\infty} \omega \langle \xi_f(\omega) \hat{\phi}_f(\omega') \rangle e^{-it(\omega+\omega')} d\omega d\omega' \right. \\ & \left. + \frac{\gamma_f}{2\pi^2} \iint_{-\infty}^{\infty} \omega \omega' \langle \hat{\phi}_f(\omega) \hat{\phi}_f(\omega') \rangle e^{-it(\omega+\omega')} d\omega d\omega' \right). \end{aligned} \quad (\text{E.13})$$

The expectation values in the above expression are now computed similarly as above in Sec. D, by using $\langle \xi_f(\omega) \xi_f(\omega') \rangle = 2\pi \delta(\omega + \omega') S_f(\omega)$, and the frequency domain result Eq. (E.6). This quickly yields

$$\langle \dot{Q} \rangle = \sum_{f \in [h, c]} \frac{\alpha_{fa}}{\alpha_f} \left(\frac{1}{2i\pi} \int_{-\infty}^{\infty} \omega G_{ff}^*(\omega) S_f(\omega) d\omega + \frac{\gamma_f}{\pi} \int_{-\infty}^{\infty} \omega^2 \left\{ |G_{ff}(\omega)|^2 S_f(\omega) + |G_{f \neq f'}(\omega)|^2 S_{f'}(\omega) \right\} d\omega \right), \quad (\text{E.14})$$

which can be evaluated numerically. The efficiency of the device is now defined, as given by Eq. (29) in the main text.

References

- [1] W. P. Schleich, K. S. Ranade, C. Anton, M. Arndt, M. Aspelmeyer, M. Bayer, G. Berg, T. Calarco, E. Fuchs, Harald and Giacobino, M. Grassl, W. M. Hänggi, Peter and Heckl, I.-V. Hertel *et al.*, *Quantum technology: from research to application*, Applied Physics B **122**(5), 130 (2016), doi:[10.1007/s00340-016-6353-8](https://doi.org/10.1007/s00340-016-6353-8).
- [2] P. Krantz, M. Kjaergaard, F. Yan, T. P. Orlando, S. Gustavsson and W. D. Oliver, *A quantum engineer's guide to superconducting qubits*, Applied Physics Reviews **6**(2), 021318 (2019), doi:[10.1063/1.5089550](https://doi.org/10.1063/1.5089550), https://pubs.aip.org/aip/apr/article-pdf/doi/10.1063/1.5089550/16667201/021318_1_online.pdf.
- [3] L. DiCarlo, J. M. Chow, J. M. Gambetta, L. S. Bishop, B. R. Johnson, D. I. Schuster, J. Majer, A. Blais, L. Frunzio, S. M. Girvin and R. J. Schoelkopf, *Demonstration of two-qubit algorithms with a superconducting quantum processor*, Nature **460**(7252), 240 (2009), doi:[10.1038/nature08121](https://doi.org/10.1038/nature08121).
- [4] E. Lucero, R. Barends, Y. Chen, J. Kelly, M. Mariantoni, A. Megrant, P. O'Malley, D. Sank, A. Vainsencher, J. Wenner, T. White, Y. Yin *et al.*, *Computing prime factors with a josephson phase qubit quantum processor*, Nature Physics **8**(10), 719 (2012), doi:[10.1038/nphys2385](https://doi.org/10.1038/nphys2385).
- [5] Y. Zheng, C. Song, M.-C. Chen, B. Xia, W. Liu, Q. Guo, L. Zhang, D. Xu, H. Deng, K. Huang, Y. Wu, Z. Yan *et al.*, *Solving systems of linear equations with a superconducting quantum processor*, Phys. Rev. Lett. **118**, 210504 (2017), doi:[10.1103/PhysRevLett.118.210504](https://doi.org/10.1103/PhysRevLett.118.210504).
- [6] M.-C. Chen, M. Gong, X. Xu, X. Yuan, J.-W. Wang, C. Wang, C. Ying, J. Lin, Y. Xu, Y. Wu, S. Wang, H. Deng *et al.*, *Demonstration of adiabatic variational quantum computing with a superconducting quantum coprocessor*, Phys. Rev. Lett. **125**, 180501 (2020), doi:[10.1103/PhysRevLett.125.180501](https://doi.org/10.1103/PhysRevLett.125.180501).
- [7] M. P. Harrigan, K. J. Sung, M. Neeley, K. J. Satzinger, F. Arute, K. Arya, J. Atalaya, J. C. Bardin, R. Barends, S. Boixo, M. Broughton, B. B. Buckley *et al.*, *Quantum approximate optimization of non-planar graph problems on a planar superconducting processor*, Nature Physics **17**(3), 332 (2021), doi:[10.1038/s41567-020-01105-y](https://doi.org/10.1038/s41567-020-01105-y).
- [8] C. J. Axline, L. D. Burkhardt, W. Pfaff, M. Zhang, K. Chou, P. Campagne-Ibarcq, P. Reinhold, L. Frunzio, S. M. Girvin, L. Jiang, M. H. Devoret and R. J. Schoelkopf, *On-demand quantum state transfer and entanglement between remote microwave cavity memories*, Nature Physics **14**(7), 705 (2018), doi:[10.1038/s41567-018-0115-y](https://doi.org/10.1038/s41567-018-0115-y).

- [9] P. Kurpiers, P. Magnard, T. Walter, B. Royer, M. Pechal, J. Heinsoo, Y. Salathé, A. Akin, S. Storz, J.-C. Besse, S. Gasparinetti, A. Blais *et al.*, *Deterministic quantum state transfer and remote entanglement using microwave photons*, *Nature* **558**(7709), 264 (2018), doi:[10.1038/s41586-018-0195-y](https://doi.org/10.1038/s41586-018-0195-y).
- [10] S. Pogorzalek, K. G. Fedorov, M. Xu, A. Parra-Rodriguez, M. Sanz, M. Fischer, E. Xie, K. Inomata, Y. Nakamura, E. Solano, A. Marx, F. Deppe *et al.*, *Secure quantum remote state preparation of squeezed microwave states*, *Nature Communications* **10**(1), 2604 (2019), doi:[10.1038/s41467-019-10727-7](https://doi.org/10.1038/s41467-019-10727-7).
- [11] K. G. Fedorov, M. Renger, S. Pogorzalek, R. D. Candia, Q. Chen, Y. Nojiri, K. Inomata, Y. Nakamura, M. Partanen, A. Marx, R. Gross and F. Deppe, *Experimental quantum teleportation of propagating microwaves*, *Science Advances* **7**(52), eabk0891 (2021), doi:[10.1126/sciadv.abk0891](https://doi.org/10.1126/sciadv.abk0891), <https://www.science.org/doi/pdf/10.1126/sciadv.abk0891>.
- [12] D. L. Underwood, W. E. Shanks, J. Koch and A. A. Houck, *Low-disorder microwave cavity lattices for quantum simulation with photons*, *Phys. Rev. A* **86**, 023837 (2012), doi:[10.1103/PhysRevA.86.023837](https://doi.org/10.1103/PhysRevA.86.023837).
- [13] A. A. Abdumalikov Jr, J. M. Fink, K. Juliusson, M. Pechal, S. Berger, A. Wallraff and S. Filipp, *Experimental realization of non-abelian non-adiabatic geometric gates*, *Nature* **496**(7446), 482 (2013), doi:[10.1038/nature12010](https://doi.org/10.1038/nature12010).
- [14] P. Roushan, C. Neill, A. Megrant, Y. Chen, R. Babbush, R. Barends, B. Campbell, Z. Chen, B. Chiaro, A. Dunsworth, A. Fowler, E. Jeffrey *et al.*, *Chiral ground-state currents of interacting photons in a synthetic magnetic field*, *Nature Physics* **13**(2), 146 (2017), doi:[10.1038/nphys3930](https://doi.org/10.1038/nphys3930).
- [15] A. J. Kollár, M. Fitzpatrick and A. A. Houck, *Hyperbolic lattices in circuit quantum electrodynamics*, *Nature* **571**(7763), 45 (2019), doi:[10.1038/s41586-019-1348-3](https://doi.org/10.1038/s41586-019-1348-3).
- [16] R. Ma, B. Saxberg, C. Owens, N. Leung, Y. Lu, J. Simon and D. I. Schuster, *A dissipatively stabilized mott insulator of photons*, *Nature* **566**(7742), 51 (2019), doi:[10.1038/s41586-019-0897-9](https://doi.org/10.1038/s41586-019-0897-9).
- [17] K. Xu, Z.-H. Sun, W. Liu, Y.-R. Zhang, H. Li, H. Dong, W. Ren, P. Zhang, F. Nori, D. Zheng, H. Fan and H. Wang, *Probing dynamical phase transitions with a superconducting quantum simulator*, *Science Advances* **6**(25), eaba4935 (2020), doi:[10.1126/sciadv.aba4935](https://doi.org/10.1126/sciadv.aba4935), <https://www.science.org/doi/pdf/10.1126/sciadv.aba4935>.
- [18] Q. Guo, C. Cheng, Z.-H. Sun, Z. Song, H. Li, Z. Wang, W. Ren, H. Dong, D. Zheng, Y.-R. Zhang, R. Mondaini, H. Fan *et al.*, *Observation of energy-resolved many-body localization*, *Nature Physics* **17**(2), 234 (2021), doi:[10.1038/s41567-020-1035-1](https://doi.org/10.1038/s41567-020-1035-1).
- [19] Q.-M. Chen, M. Fischer, Y. Nojiri, M. Renger, E. Xie, M. Partanen, S. Pogorzalek, K. G. Fedorov, A. Marx, F. Deppe and R. Gross, *Quantum behavior of the duffing oscillator at the dissipative phase transition*, *Nature Communications* **14**(1), 2896 (2023), doi:[10.1038/s41467-023-38217-x](https://doi.org/10.1038/s41467-023-38217-x).
- [20] S. Barzanjeh, S. Pirandola, D. Vitali and J. M. Fink, *Microwave quantum illumination using a digital receiver*, *Science Advances* **6**(19), eabb0451 (2020), doi:[10.1126/sciadv.abb0451](https://doi.org/10.1126/sciadv.abb0451), <https://www.science.org/doi/pdf/10.1126/sciadv.abb0451>.

- [21] A. Bienfait, P. Campagne-Ibarcq, A. H. Kiilerich, X. Zhou, S. Probst, J. J. Pla, T. Schenkel, D. Vion, D. Esteve, J. J. L. Morton, K. Moelmer and P. Bertet, *Magnetic resonance with squeezed microwaves*, Phys. Rev. X **7**, 041011 (2017), doi:[10.1103/PhysRevX.7.041011](https://doi.org/10.1103/PhysRevX.7.041011).
- [22] Z. Wang, M. Xu, X. Han, W. Fu, S. Puri, S. M. Girvin, H. X. Tang, S. Shankar and M. H. Devoret, *Quantum microwave radiometry with a superconducting qubit*, Phys. Rev. Lett. **126**, 180501 (2021), doi:[10.1103/PhysRevLett.126.180501](https://doi.org/10.1103/PhysRevLett.126.180501).
- [23] R. Kokkonen, J. Govenius, V. Vesterinen, R. E. Lake, A. M. Gunyhó, K. Y. Tan, S. Simbierowicz, L. Grönberg, J. Lehtinen, M. Prunnila, J. Hassel, A. Lamminen *et al.*, *Nanobolometer with ultralow noise equivalent power*, Communications Physics **2**(1), 124 (2019), doi:[10.1038/s42005-019-0225-6](https://doi.org/10.1038/s42005-019-0225-6).
- [24] R. Kokkonen, J.-P. Girard, D. Hazra, A. Laitinen, J. Govenius, R. E. Lake, I. Sallinen, V. Vesterinen, M. Partanen, J. Y. Tan, K. W. Chan, K. Y. Tan *et al.*, *Bolometer operating at the threshold for circuit quantum electrodynamics*, Nature **586**(7827), 47 (2020), doi:[10.1038/s41586-020-2753-3](https://doi.org/10.1038/s41586-020-2753-3).
- [25] J. Govenius, R. E. Lake, K. Y. Tan and M. Möttönen, *Detection of zeptojoule microwave pulses using electrothermal feedback in proximity-induced josephson junctions*, Phys. Rev. Lett. **117**, 030802 (2016), doi:[10.1103/PhysRevLett.117.030802](https://doi.org/10.1103/PhysRevLett.117.030802).
- [26] S. Gasparinetti, K. L. Viisanen, O.-P. Saira, T. Faivre, M. Arzeo, M. Meschke and J. P. Pekola, *Fast electron thermometry for ultrasensitive calorimetric detection*, Phys. Rev. Appl. **3**, 014007 (2015), doi:[10.1103/PhysRevApplied.3.014007](https://doi.org/10.1103/PhysRevApplied.3.014007).
- [27] S. Deffner and S. Campbell, *Quantum Thermodynamics*, 2053-2571. Morgan and Claypool Publishers, ISBN 978-1-64327-658-8, doi:[10.1088/2053-2571/ab21c6](https://doi.org/10.1088/2053-2571/ab21c6) (2019).
- [28] J. Goold, M. Huber, A. Riera, L. del Rio and P. Skrzypczyk, *The role of quantum information in thermodynamics—a topical review*, Journal of Physics A: Mathematical and Theoretical **49**(14), 143001 (2016), doi:[10.1088/1751-8113/49/14/143001](https://doi.org/10.1088/1751-8113/49/14/143001).
- [29] J. Gemmer, M. Michel and G. Mahler, *Quantum Thermodynamics: Emergence of Thermodynamic Behavior Within Composite Quantum Systems*, Lecture Notes in Physics. Springer Berlin Heidelberg, ISBN 9783540229117 (2004).
- [30] T. Uusnäkki, T. Mörstedt, W. Teixeira, M. Rasola and M. Möttönen, *Experimental realization of a quantum heat engine based on dissipation-engineered superconducting circuits* (2025), [2502.20143](https://arxiv.org/abs/2502.20143).
- [31] S. Sundelin, M. A. Aamir, V. M. Kulkarni, C. Castillo-Moreno and S. Gasparinetti, *Quantum refrigeration powered by noise in a superconducting circuit* (2024), [2403.03373](https://arxiv.org/abs/2403.03373).
- [32] J. Roßnagel, S. T. Dawkins, K. N. Tolazzi, O. Abah, E. Lutz, F. Schmidt-Kaler and K. Singer, *A single-atom heat engine*, Science **352**(6283), 325 (2016), doi:[10.1126/science.aad6320](https://doi.org/10.1126/science.aad6320), [1510.03681](https://arxiv.org/abs/1510.03681).
- [33] D. von Lindenfels, O. Gräß, C. T. Schmiegelow, V. Kaushal, J. Schulz, M. T. Mitchison, J. Goold, F. Schmidt-Kaler and U. G. Poschinger, *Spin heat engine coupled to a harmonic-oscillator flywheel*, Phys. Rev. Lett. **123**, 080602 (2019), doi:[10.1103/PhysRevLett.123.080602](https://doi.org/10.1103/PhysRevLett.123.080602).
- [34] N. Van Horne, D. Yum, T. Dutta, P. Hänggi, J. Gong, D. Poletti and M. Mukherjee, *Single-atom energy-conversion device with a quantum load*, npj Quantum Information **6**, 37 (2020), doi:[10.1038/s41534-020-0264-6](https://doi.org/10.1038/s41534-020-0264-6).

- [35] J. Klatzow, J. N. Becker, P. M. Ledingham, C. Weinzetl, K. T. Kaczmarek, D. J. Saunders, J. Nunn, I. A. Walmsley, R. Uzdin and E. Poem, *Experimental demonstration of quantum effects in the operation of microscopic heat engines*, Phys. Rev. Lett. **122**, 110601 (2019), doi:[10.1103/PhysRevLett.122.110601](https://doi.org/10.1103/PhysRevLett.122.110601).
- [36] R. J. de Assis, T. M. de Mendonça, C. J. Villas-Boas, A. M. de Souza, R. S. Sarthour, I. S. Oliveira and N. G. de Almeida, *Efficiency of a quantum otto heat engine operating under a reservoir at effective negative temperatures*, Phys. Rev. Lett. **122**, 240602 (2019), doi:[10.1103/PhysRevLett.122.240602](https://doi.org/10.1103/PhysRevLett.122.240602).
- [37] J. P. S. Peterson, T. B. Batalhão, M. Herrera, A. M. Souza, R. S. Sarthour, I. S. Oliveira and R. M. Serra, *Experimental characterization of a spin quantum heat engine*, Phys. Rev. Lett. **123**, 240601 (2019), doi:[10.1103/PhysRevLett.123.240601](https://doi.org/10.1103/PhysRevLett.123.240601).
- [38] Q. Bouton, J. Nettersheim, S. Burgardt, D. Adam, E. Lutz and A. Widera, *A quantum heat engine driven by atomic collisions*, Nature Communications **12**(1), 2063 (2021), doi:[10.1038/s41467-021-22222-z](https://doi.org/10.1038/s41467-021-22222-z).
- [39] J. P. Pekola and F. W. J. Hekking, *Normal-metal-superconductor tunnel junction as a brownian refrigerator*, Phys. Rev. Lett. **98**, 210604 (2007), doi:[10.1103/PhysRevLett.98.210604](https://doi.org/10.1103/PhysRevLett.98.210604).
- [40] J. P. Pekola, *Towards quantum thermodynamics in electronic circuits*, Nature Physics **11**(2), 118 (2015), doi:[10.1038/nphys3169](https://doi.org/10.1038/nphys3169).
- [41] B. Karimi and J. P. Pekola, *Otto refrigerator based on a superconducting qubit: Classical and quantum performance*, Phys. Rev. B **94**, 184503 (2016), doi:[10.1103/PhysRevB.94.184503](https://doi.org/10.1103/PhysRevB.94.184503).
- [42] G. Thomas, A. Gubaydullin, D. S. Golubev and J. P. Pekola, *Thermally pumped on-chip maser*, Phys. Rev. B **102**, 104503 (2020), doi:[10.1103/PhysRevB.102.104503](https://doi.org/10.1103/PhysRevB.102.104503).
- [43] A. Ronzani, B. Karimi, J. Senior, Y.-C. Chang, J. T. Peltonen, C. Chen and J. P. Pekola, *Tunable photonic heat transport in a quantum heat valve*, Nature Physics **14**(10), 991 (2018), doi:[10.1038/s41567-018-0199-4](https://doi.org/10.1038/s41567-018-0199-4).
- [44] K. Y. Tan, M. Partanen, R. E. Lake, J. Govenius, S. Masuda and M. Möttönen, *Quantum-circuit refrigerator*, Nature Communications **8**(1), 15189 (2017), doi:[10.1038/ncomms15189](https://doi.org/10.1038/ncomms15189).
- [45] M. Rasola and M. Möttönen, *Autonomous quantum heat engine based on non-markovian dynamics of an optomechanical hamiltonian*, Scientific Reports **14**(1), 9448 (2024), doi:[10.1038/s41598-024-59881-z](https://doi.org/10.1038/s41598-024-59881-z).
- [46] S. Barzanjeh, A. Xuereb, S. Groblacher, M. Paternostro, C. A. Regal and E. M. Weig, *Optomechanics for quantum technologies*, Nature Physics **18**(1), 15 (2022), doi:[10.1038/s41567-021-01402-0](https://doi.org/10.1038/s41567-021-01402-0).
- [47] M. Aspelmeyer, T. J. Kippenberg and F. Marquardt, *Cavity optomechanics*, Rev. Mod. Phys. **86**, 1391 (2014), doi:[10.1103/RevModPhys.86.1391](https://doi.org/10.1103/RevModPhys.86.1391).
- [48] M. Xu, J. T. Stockburger, G. Kurizki and J. Ankerhold, *Minimal quantum thermal machine in a bandgap environment: non-markovian features and anti-zeno advantage*, New Journal of Physics **24**(3), 035003 (2022), doi:[10.1088/1367-2630/ac575b](https://doi.org/10.1088/1367-2630/ac575b).

- [49] Y. Dong, K. Zhang, F. Bariani and P. Meystre, *Work measurement in an optomechanical quantum heat engine*, Phys. Rev. A **92**, 033854 (2015), doi:[10.1103/PhysRevA.92.033854](https://doi.org/10.1103/PhysRevA.92.033854).
- [50] K. Zhang, F. Bariani and P. Meystre, *Quantum optomechanical heat engine*, Phys. Rev. Lett. **112**, 150602 (2014), doi:[10.1103/PhysRevLett.112.150602](https://doi.org/10.1103/PhysRevLett.112.150602).
- [51] K. Zhang, F. Bariani and P. Meystre, *Theory of an optomechanical quantum heat engine*, Phys. Rev. A **90**, 023819 (2014), doi:[10.1103/PhysRevA.90.023819](https://doi.org/10.1103/PhysRevA.90.023819).
- [52] M. T. Naseem and Özgür E. Müstecaplıoğlu, *Quantum heat engine with a quadratically coupled optomechanical system*, J. Opt. Soc. Am. B **36**(11), 3000 (2019), doi:[10.1364/JOSAB.36.003000](https://doi.org/10.1364/JOSAB.36.003000).
- [53] M. Izadyari, M. Öncü, K. Durak and Özgür E. Müstecaplıoğlu, *Quantum signatures in a quadratic optomechanical heat engine with an atom in a tapered trap*, J. Opt. Soc. Am. B **39**(12), 3247 (2022), doi:[10.1364/JOSAB.472901](https://doi.org/10.1364/JOSAB.472901).
- [54] A. U. C. Hardal, N. Aslan, C. M. Wilson and O. E. Müstecaplıoğlu, *Quantum heat engine with coupled superconducting resonators*, Phys. Rev. E **96**, 062120 (2017), doi:[10.1103/PhysRevE.96.062120](https://doi.org/10.1103/PhysRevE.96.062120).
- [55] A. Mari, A. Farace and V. Giovannetti, *Quantum optomechanical piston engines powered by heat*, Journal of Physics B: Atomic, Molecular and Optical Physics **48**(17), 175501 (2015), doi:[10.1088/0953-4075/48/17/175501](https://doi.org/10.1088/0953-4075/48/17/175501).
- [56] D. Gelbwaser-Klimovsky and G. Kurizki, *Work extraction from heat-powered quantized optomechanical setups*, Scientific Reports **5**(1), 7809 (2015), doi:[10.1038/srep07809](https://doi.org/10.1038/srep07809).
- [57] D. Gelbwaser-Klimovsky, R. Alicki and G. Kurizki, *Work and energy gain of heat-pumped quantized amplifiers*, Europhysics Letters **103**(6), 60005 (2013), doi:[10.1209/0295-5075/103/60005](https://doi.org/10.1209/0295-5075/103/60005).
- [58] M. H. Devoret, *Quantum fluctuations in electrical circuits*, Edition de Physique, France, ISBN 0-444-82593-2 (1997).
- [59] U. Vool and M. Devoret, *Introduction to quantum electromagnetic circuits*, International Journal of Circuit Theory and Applications **45**(7), 897 (2017), doi:<https://doi.org/10.1002/cta.2359>, <https://onlinelibrary.wiley.com/doi/pdf/10.1002/cta.2359>.
- [60] R. Kosloff and Y. Rezek, *The quantum harmonic otto cycle*, Entropy **19**(4) (2017), doi:[10.3390/e19040136](https://doi.org/10.3390/e19040136).
- [61] B. Hall, *Quantum Theory for Mathematicians*, Graduate Texts in Mathematics. Springer New York, ISBN 9781461471165 (2013).
- [62] A. Schmid, *On a quasiclassical langevin equation*, Journal of Low Temperature Physics **49**(5), 609 (1982), doi:[10.1007/BF00681904](https://doi.org/10.1007/BF00681904).
- [63] A. A. Clerk, M. H. Devoret, S. M. Girvin, F. Marquardt and R. J. Schoelkopf, *Introduction to quantum noise, measurement, and amplification*, Rev. Mod. Phys. **82**, 1155 (2010), doi:[10.1103/RevModPhys.82.1155](https://doi.org/10.1103/RevModPhys.82.1155).
- [64] K. Kawasaki, *Simple derivations of generalized linear and nonlinear langevin equations*, Journal of Physics A: Mathematical, Nuclear and General **6**(9), 1289 (1973), doi:[10.1088/0305-4470/6/9/004](https://doi.org/10.1088/0305-4470/6/9/004).

- [65] M. Göppl, A. Fragner, M. Baur, R. Bianchetti, S. Filipp, J. M. Fink, P. J. Leek, G. Puebla, L. Steffen and A. Wallraff, *Coplanar waveguide resonators for circuit quantum electrodynamics*, Journal of Applied Physics **104**(11), 113904 (2008), doi:[10.1063/1.3010859](https://doi.org/10.1063/1.3010859), <https://doi.org/10.1063/1.3010859>.
- [66] L. Frunzio, A. Wallraff, D. Schuster, J. Majer and R. Schoelkopf, *Fabrication and characterization of superconducting circuit qed devices for quantum computation*, IEEE Transactions on Applied Superconductivity **15**(2), 860 (2005), doi:[10.1109/TASC.2005.850084](https://doi.org/10.1109/TASC.2005.850084).
- [67] R. Barends, J. J. A. Baselmans, J. N. Hovenier, J. R. Gao, S. J. C. Yates, T. M. Klapwijk and H. F. C. Hoevers, *Niobium and tantalum high q resonators for photon detectors*, IEEE Transactions on Applied Superconductivity **17**(2), 263 (2007), doi:[10.1109/TASC.2007.898541](https://doi.org/10.1109/TASC.2007.898541).
- [68] E. V. Zikiy, A. I. Ivanov, N. S. Smirnov, D. O. Moskalev, A. R. Polozov, V. I. and Matanin, E. I. Malevannaya, V. V. Echeistov, T. G. Konstantinova and I. A. Rodionov, *High-q trenching aluminum coplanar resonators with an ultrasonic edge microcutting for superconducting quantum devices*, Scientific Reports **13**(1), 15536 (2023), doi:[10.1038/s41598-023-42332-6](https://doi.org/10.1038/s41598-023-42332-6).
- [69] M. Rasola, S. Klaver, J. Ma, P. Singh, T. Uusnäkki, H. Suominen and M. Möttönen, *Low-characteristic-impedance superconducting tadpole resonators in the sub-gigahertz regime*, Phys. Rev. Res. **6**, 043297 (2024), doi:[10.1103/PhysRevResearch.6.043297](https://doi.org/10.1103/PhysRevResearch.6.043297).
- [70] A. Keränen, Q.-M. Chen, A. Gunyhó, P. Singh, J. Ma, V. Vesterinen, J. Govenius and M. Möttönen, *Correlation measurement of propagating microwave photons at millikelvin*, Nature Communications **16**(1), 3875 (2025), doi:[10.1038/s41467-025-59230-2](https://doi.org/10.1038/s41467-025-59230-2).
- [71] A. Blais, A. L. Grimsmo, S. M. Girvin and A. Wallraff, *Circuit quantum electrodynamics*, Rev. Mod. Phys. **93**, 025005 (2021), doi:[10.1103/RevModPhys.93.025005](https://doi.org/10.1103/RevModPhys.93.025005).
- [72] J. Pekola and I. Khaymovich, *Thermodynamics in single-electron circuits and superconducting qubits*, Annual Review of Condensed Matter Physics **10**(1), 193 (2019), doi:[10.1146/annurev-conmatphys-033117-054120](https://doi.org/10.1146/annurev-conmatphys-033117-054120), <https://doi.org/10.1146/annurev-conmatphys-033117-054120>.
- [73] T. F. Mörstedt, A. Viitanen, V. Vadimov, V. Sevriuk, M. Partanen, E. Hyppä, G. Catelani, M. Silveri, K. Y. Tan and M. Möttönen, *Recent developments in quantum-circuit refrigeration*, Annalen der Physik **534**(7), 2100543 (2022), doi:<https://doi.org/10.1002/andp.202100543>, <https://onlinelibrary.wiley.com/doi/pdf/10.1002/andp.202100543>.
- [74] A. Viitanen, T. Mörstedt, W. S. Teixeira, M. Tiiri, J. Rabinä, M. Silveri and M. Möttönen, *Quantum-circuit refrigeration of a superconducting microwave resonator well below a single quantum*, Phys. Rev. Res. **6**, 023262 (2024), doi:[10.1103/PhysRevResearch.6.023262](https://doi.org/10.1103/PhysRevResearch.6.023262).
- [75] H. Kivijärvi, A. Viitanen, T. Mörstedt and M. Möttönen, *Noise-induced quantum-circuit refrigeration* (2024), [2412.05886](https://arxiv.org/abs/2412.05886).
- [76] T. F. Mörstedt, W. S. Teixeira, A. Viitanen, H. Kivijärvi, M. Tiiri, M. Rasola, A. M. Gunyho, S. Kundu, L. Lattier, V. Vadimov, G. Catelani, V. Sevriuk et al., *Rapid on-demand generation of thermal states in superconducting quantum circuits* (2024), [2402.09594](https://arxiv.org/abs/2402.09594).
- [77] B. Datta, *Numerical Linear Algebra and Applications: Second Edition*, Other Titles in Applied Mathematics. Society for Industrial and Applied Mathematics (SIAM, 3600 Market Street, Floor 6, Philadelphia, PA 19104), ISBN 9780898717655 (2010).